









Binary black hole mergers from Population III stars: uncertainties from star formation and binary star properties

Filippo Santoliquido^{1,2}★, Michela Mapelli^{1,2,3}†, Giuliano Iorio^{1,2,3}‡, Guglielmo Costa^{1,2,3,4},
Simon C. O. Glover⁵, Tilman Hartwig^{6,7,8}, Ralf S. Klessen⁵, and Lorenzo Merli¹

¹Physics and Astronomy Department Galileo Galilei, University of Padova, Vicolo dell'Osservatorio 3, I-35122, Padova, Italy

²INFN–Padova, Via Marzolo 8, I-35131, Padova, Italy

³INAF–Osservatorio Astronomico di Padova, Vicolo dell'Osservatorio 5, I-35122, Padova, Italy

⁴Univ Lyon, Univ Lyon1, Ens de Lyon, CNRS, Centre de Recherche Astrophysique de Lyon UMR5574, F-69230, Saint-Genis-Laval, France

⁵Universität Heidelberg, Zentrum für Astronomie, Institut für Theoretische Astrophysik, Albert-Ueberle-Str. 2, D-69120 Heidelberg, Germany

⁶Department of Physics, School of Science, The University of Tokyo, Bunkyo, Tokyo 113-0033, Japan

⁷Institute for Physics of Intelligence, School of Science, The University of Tokyo, Bunkyo, Tokyo 113-0033, Japan

⁸Kavli Institute for the Physics and Mathematics of the Universe (WPI), The University of Tokyo Institutes for Advanced Study, The University of Tokyo, Kashiwa, Chiba 277-8583, Japan

Accepted XXX. Received YYY; in original form ZZZ

ABSTRACT

Population III (Pop. III) binary stars likely produced the first stellar-born binary black hole (BBH) mergers in the Universe. Here, we quantify the main sources of uncertainty for the merger rate density evolution and mass spectrum of Pop. III BBHs by considering four different formation histories and 11 models of the initial orbital properties of Pop. III binary stars. The uncertainty on the orbital properties affects the BBH merger rate density by up to two orders of magnitude, models with shorter orbital periods leading to higher BBH merger rates. The uncertainty on the star formation history has a substantial impact on both the shape and the normalisation of the BBH merger rate density: the peak of the merger rate density shifts from $z \sim 8$ up to $z \sim 16$ depending on the assumed star formation rate, while the maximum BBH merger rate density for our fiducial binary population model spans from ~ 2 to $\sim 30 \text{ Gpc}^{-3} \text{ yr}^{-1}$. The typical BBH masses are not affected by the star formation rate model and only mildly influenced by the binary population parameters. The primary black holes born from Pop. III stars tend to be rather massive ($30 - 40 M_{\odot}$) with respect to those born from metal-rich stars ($8 - 10 M_{\odot}$). We estimate that the Einstein Telescope will detect $10 - 10^4$ Pop. III BBH mergers per year, depending on the star formation history and binary star properties.

Key words: stars: Population III – gravitational waves – black hole physics – galaxies: star formation – methods: numerical

1 INTRODUCTION

The third-generation ground-based gravitational-wave (GW) interferometers, the Einstein Telescope (Punturo et al. 2010) and Cosmic Explorer (Reitze et al. 2019), will capture binary black hole (BBH) mergers up to a redshift $z \sim 100$ (Maggiore et al. 2020; Ng et al. 2021, 2022b), with a factor of ~ 100 higher sensitivity at 10 Hz with respect to current detectors (Maggiore et al. 2020; Kalogera et al. 2021). Hence, they will be the ideal observatories to probe the merger of stellar-sized black holes (BHs) in the early Universe (e.g., Ng et al. 2021; Singh et al. 2022; Ng et al. 2022a), such as primordial BHs, and BHs born from Population III (hereafter, Pop. III) stars.

Here, we will focus on BHs born from the collapse of Pop. III stars, i.e. the first, metal-free stars (Haiman et al. 1996; Tegmark et al. 1997; Yoshida et al. 2003). While we have not directly observed them yet, we expect that Pop. III stars gave a key contribution to the reionization

of the Universe (Kitayama et al. 2004; Alvarez et al. 2006; Johnson et al. 2007) and to the enrichment of the intergalactic medium, by spreading metals heavier than He through supernova explosions (e.g., Madau & Rees 2001; Bromm & Loeb 2003; Tornatore et al. 2007; Karlsson et al. 2008; Bromm et al. 2009; Karlsson et al. 2013).

Mergers of BHs from Pop. III stars have attracted a considerable interest (e.g., Kinugawa et al. 2014, 2016; Hartwig et al. 2016; Belczynski et al. 2017; Tanikawa et al. 2022a) since the first LIGO–Virgo detection of a BBH merger, GW150914, with a total mass of $65.3^{+4.1}_{-3.4} M_{\odot}$ in the source frame (Abbott et al. 2016a; Abbott et al. 2016b). In fact, BHs from Pop. III stars are expected to extend to higher masses than the compact remnants of Population I stars (hereafter, Pop. I stars, i.e. metal-rich stars like our Sun) because mass loss by stellar winds is drastically quenched in metal-free stars (e.g., Madau & Rees 2001; Heger et al. 2002; Woosley et al. 2002; Schneider et al. 2002; Kinugawa et al. 2014; Volpato et al. 2023). Moreover, the initial mass function of Pop. III stars is commonly believed to be more top heavy than that of Pop. I stars (e.g., Abel et al. 2002; Bromm & Larson 2004; Schneider et al. 2006; Yoshida et al. 2006; Stacy & Bromm 2013; Bromm 2013; Glover 2013; Susa

★ E-mail: filippo.santoliquido@unipd.it (FS)

† E-mail: michela.mapelli@unipd.it

‡ E-mail: giuliano.iorio@unipd.it

et al. 2014; Hirano et al. 2014, 2015; Wollenberg et al. 2020; Chon et al. 2021; Tanikawa et al. 2021b; Jaura et al. 2022; Prole et al. 2022; Klessen & Glover 2023), increasing the efficiency of BH formation. Also, Pop. III binary stars tend to produce massive BBHs because they are more likely to experience stable mass transfer than Pop. I binary stars. In fact, massive Pop. III stars tend to have radiative envelopes for most of their life, avoiding common-envelope episodes (Kinugawa et al. 2016; Inayoshi et al. 2017).

For the above reasons, Pop. III stars are among the main suspects for the formation of BHs inside or above the pair-instability mass gap (e.g., Liu & Bromm 2020c; Farrell et al. 2021; Kinugawa et al. 2021; Tanikawa et al. 2021b, 2022a), possibly explaining the formation of the peculiar merger GW190521, with primary (secondary) BH mass 85^{+21}_{-14} (66^{+17}_{-18}) M_{\odot} (Abbott et al. 2020a,b).

Despite this revived interest in Pop. III stars and their remnants, the actual merger rate density and mass spectrum of Pop. III BHs are still debated (e.g., Kinugawa et al. 2016; Belczynski et al. 2017; Kinugawa et al. 2020), mostly because of the absence of direct evidence for Pop. III stars. Current predictions yield a local merger rate density of Pop. III BBHs ranging from $\sim 10^{-1}$ to $\sim 10^2$ $\text{yr}^{-1} \text{Gpc}^{-3}$ (Kinugawa et al. 2014; Belczynski et al. 2017; Liu & Bromm 2020a; Tanikawa et al. 2022a). This uncertainty comes from different assumptions regarding the initial binary properties, star and binary evolution processes, and star formation rate history. Moreover, dynamical interactions of Pop. III BHs might also contribute to the merger rate (e.g., Liu & Bromm 2020a; Wang et al. 2022). All of these uncertainties propagate into the redshift evolution of the mass spectrum and merger rate.

Here, we quantify the current uncertainties on the merger rate density and mass spectrum of BBH mergers from Pop. III stars by considering a wide range of assumptions for the star formation history of metal-free stars (Jaacks et al. 2019; Liu & Bromm 2020b; Skinner & Wise 2020; Hartwig et al. 2022), for their initial binary properties (e.g., Larson 1998; Stacy & Bromm 2013; Stacy et al. 2016; Tanikawa et al. 2022a), and binary evolution (e.g., Costa et al. 2023, and references therein), by adopting the `SEVN` binary population synthesis code (Spera et al. 2019; Mapelli et al. 2020; Iorio et al. 2023).

2 METHODS

2.1 Population synthesis with SEVN

We derived our BBH merger catalogues with the binary population synthesis code `SEVN`, which integrates single and binary evolution by interpolating a set of pre-computed single stellar-evolution tracks, as described in Iorio et al. (2023). Here, we adopt the following set-up of `SEVN`. We calculated the Pop. III stellar tracks with the `PARSEC` code (Bressan et al. 2012; Costa et al. 2021; Nguyen et al. 2022) at metallicity $Z = 10^{-11}$. Here and in the rest of the manuscript, Z is the mass fraction of elements heavier than helium, in absolute units. This value of Z is equivalent to considering a metal-free composition (e.g., Marigo et al. 2001; Tanikawa et al. 2021b). The zero-age main sequence mass ($ZAMS$) of our tracks ranges from 2 to 600 M_{\odot} . Tracks with $2 < M_{ZAMS}/M_{\odot} < 8$ evolve until the end of the core He burning and reach the early asymptotic giant branch phase, whereas tracks with $M_{ZAMS} > 8 M_{\odot}$ evolve until the beginning of the core O burning phase. Our tracks do not include stellar rotation and are computed with the same physical set-up as described by Costa et al. (2021) for stellar winds, nuclear reaction network, opacity and equation of state. Above the convective core, we adopt a penetrative

overshooting with a characteristic parameter of $\Lambda_{\text{ov}} = 0.5$ in units of pressure scale height. We refer to Costa et al. (2023) for more details on the evolutionary tracks. In Section 4, we compare the main features of our models with alternative Pop. III models (Tanikawa et al. 2021a, 2022b). We explore the uncertainties connected with different sets of stellar evolution models in a forthcoming work.

Even if our initial stellar models are non spinning, `SEVN` includes a formalism for spin up and down via tides and mass accretion, based on Hurley et al. (2002). However, we did not incorporate an accurate treatment for angular momentum transport in the stellar interior (Talon & Zahn 1997; Maeder & Zahn 1998; Spruit 2002) and we do not account for other processes that can affect the spin of the newly born compact object during core collapse (e.g., the onset of an accretion disc). Hence, we will not discuss BH spin magnitudes here.

We remap the final properties of the stars (in particular, final total mass and CO core mass) into BH masses by adopting the rapid model for core-collapse supernovae (Fryer et al. 2012). Furthermore, we implement the outcome of electron-capture supernovae, as detailed in Giacobbo & Mapelli (2019). For (pulsational) pair-instability supernovae, we adopt the model presented in Mapelli et al. (2020). In this model, based on the hydro-dynamical calculation by Woosley (2017) (see also Spera & Mapelli 2017), a star undergoes pulsational pair instability if the pre-supernova He-core mass, M_{He} , is between 32 and 64 M_{\odot} . The mass of the BH after pulsational pair instability is:

$$M_{\text{BH}} = \begin{cases} \alpha_{\text{P}} M_{\text{CCSN}} & \text{if } (\alpha_{\text{P}} M_{\text{CCSN}}) \geq 4.5 M_{\odot} \\ 0 & \text{if } (\alpha_{\text{P}} M_{\text{CCSN}}) < 4.5 M_{\odot}, \end{cases} \quad (1)$$

where M_{CCSN} is the mass of the BH after a core-collapse supernova (without pulsational pair instability) and α_{P} is a dimensionless correction factor between 0 and 1. The dimensionless factor α_{P} depends on M_{He} and the pre-supernova mass ratio between the mass of the He core and the total stellar mass (see Equations 4 and 5 in the Appendix of Mapelli et al. 2020). For $M_{\text{He}} > 64 M_{\odot}$, the star enters the pair-instability regime, and we assume that (i) the star is completely disrupted and leaves no compact remnant if $M_{\text{He}} \leq 135 M_{\odot}$; (ii) the star directly collapses to a BH if $M_{\text{He}} > 135 M_{\odot}$ (see Costa et al. 2023 and Iorio et al. 2023 for more details on these assumptions).

Here, we draw BH natal kicks from two different distributions. In our fiducial case, we adopt the formalism by Giacobbo & Mapelli (2020, hereafter `GM20`):

$$V_{\text{kick}} = f_{\text{H05}} \frac{\langle M_{\text{NS}} \rangle}{M_{\text{rem}}} \frac{M_{\text{ej}}}{\langle M_{\text{ej}} \rangle}, \quad (2)$$

where $\langle M_{\text{NS}} \rangle$ and $\langle M_{\text{ej}} \rangle$ are the average neutron star mass and ejecta mass from single stellar evolution, respectively, while M_{rem} and M_{ej} are the compact object mass and the ejecta mass. The term f_{H05} is a random number drawn from a Maxwellian distribution with one-dimensional root mean square $\sigma_{\text{kick}} = 265 \text{ km s}^{-1}$, coming from a fit to the proper motions of 73 young pulsars ($< 3 \text{ Myr}$) in the Milky Way (Hobbs et al. 2005). In this formalism, stripped and ultra-stripped supernovae result in lower kicks with respect to the other explosions, owing to the lower amount of ejected mass M_{ej} (Bray & Eldridge 2016, 2018). BHs originating from a direct collapse receive zero natal kicks.

In the alternative model we present in Section 4, we randomly draw the BH natal kicks from a Maxwellian distribution with one dimensional root mean square $\sigma_{\text{kick}} = 150 \text{ km s}^{-1}$ (hereafter σ_{150}). This model matches the BH kicks inferred by Atri et al. (2019), based on the proper motions of 16 BH X-ray binaries in the Milky Way. The two models `GM20` and σ_{150} bracket the uncertainties on BH natal kicks. While the latter is independent of the mass of the BH,

the former introduces a strong dependence on both the mass of the compact remnant (M_{rem}) and the evolution of the progenitor star (encoded in M_{ej}).

In addition to the natal kick, we also calculate a Blaauw kick (Blaauw 1961) resulting from the instantaneous mass loss in a binary system triggered by a supernova explosion. We use the same formalism as described in Appendix A of Hurley et al. (2002).

Finally, `SEVN` integrates the following binary evolution processes: wind mass transfer, stable Roche-lobe overflow, common envelope evolution (adopting the α formalism, Hurley et al. 2002), tidal evolution, stellar collisions, magnetic braking, and GW decay (Iorio et al. 2023).

Here, we use the same set-up as the fiducial model of Iorio et al. (2023), adopting the default values for all relevant parameters (Section 3.2 of Iorio et al. 2023): mass transfer is always stable for main sequence and Hertzsprung-gap donor stars, while we follow the prescriptions by Hurley et al. (2002) in all the other cases. We set the Roche-lobe overflow mass accretion efficiency to 0.5 for a non-degenerate accretor, and assume that the mass which is not accreted is lost from the vicinity of the accretor as an isotropic wind (isotropic re-emission). At the onset of the Roche-lobe overflow, `SEVN` circularises the orbit at periastron. During common envelope, we estimate the envelope binding energy using the same formalism as in Claeys et al. (2014). We adopt $\alpha = 1$ for the common-envelope efficiency parameter, i.e. we assume that all the kinetic energy lost from the system contributes to unbinding the common envelope. In Appendix B, we discuss the impact of different assumptions for mass accretion and common-envelope efficiency.

2.2 Initial conditions for Pop. III binary systems

We use the same binary-population synthesis simulations as in Costa et al. (2023). We summarise their initial conditions here below and in Table 1.

2.2.1 Initial mass function (IMF)

Among the many different models proposed in the literature, we consider the following four distributions for the initial mass function (IMF), because they bracket the uncertainties on the IMF of Pop. III stars (e.g., Bromm & Larson 2004; Yoshida et al. 2006; Bromm 2013; Glover 2013).

- A flat-in-log probability distribution function $\xi(M_{\text{ZAMS}})$ (see e.g. Stacy & Bromm 2013; Susa et al. 2014; Hirano et al. 2014, 2015; Wollenberg et al. 2020; Chon et al. 2021; Tanikawa et al. 2021b; Jaura et al. 2022; Prole et al. 2022):

$$\xi(M_{\text{ZAMS}}) \propto M_{\text{ZAMS}}^{-1}. \quad (3)$$

- A Kroupa (2001) distribution (hereafter K01):

$$\xi(M_{\text{ZAMS}}) \propto M_{\text{ZAMS}}^{-2.3}. \quad (4)$$

With respect to the original K01, which has a flatter slope for $M_{\text{ZAMS}} < 0.5 M_{\odot}$, here we assume a single slope because we do not generate ZAMS masses $< 5 M_{\odot}$ from this distribution.

- A Larson (1998) distribution (hereafter L98):

$$\xi(M_{\text{ZAMS}}) \propto M_{\text{ZAMS}}^{-2.35} e^{-M_{\text{cut1}}/M_{\text{ZAMS}}}, \quad (5)$$

where $M_{\text{cut1}} = 20 M_{\odot}$ (Valiante et al. 2016).

- A top-heavy distribution (hereafter TOP), following Stacy & Bromm (2013), Jaacks et al. (2019), and Liu & Bromm (2020a):

$$\xi(M_{\text{ZAMS}}) \propto M_{\text{ZAMS}}^{-0.17} e^{-M_{\text{cut2}}^2/M_{\text{ZAMS}}^2}, \quad (6)$$

where $M_{\text{cut2}} = 20 M_{\odot}$.

In the following, we call LOG, KRO, LAR, and TOP our models adopting the flat-in-log, K01, L98, and top-heavy IMFs, respectively (Table 1). In all of our models but LOG3 (Table 1), we use the aforementioned IMFs to generate the ZAMS mass of the primary star $M_{\text{ZAMS},1}$ (i.e., the most massive component of the binary star) in the range $[5, 550] M_{\odot}$. In model LOG3, we instead randomly sample the entire IMF (both primary and secondary stars) in the range $M_{\text{ZAMS}} \in [5, 550] M_{\odot}$ according to the LOG IMF.

2.2.2 Mass ratio and secondary mass

We draw the mass of the secondary star ($M_{\text{ZAMS},2}$) according to three different distributions.

- We use the distribution of the mass ratio $q = M_{\text{ZAMS},2}/M_{\text{ZAMS},1}$ from Sana et al. (2012, hereafter S12):

$$\xi(q) \propto q^{-0.1} \text{ with } q \in [0.1, 1] \text{ and } M_{\text{ZAMS},2} \geq 2.2 M_{\odot}. \quad (7)$$

This distribution is a fit to the mass ratio of O- and B-type binary stars in the local Universe.

- In the sorted distribution, we draw the ZAMS mass of the entire stellar population from the same IMF, and then we randomly pair two stars from this distribution, imposing that $M_{\text{ZAMS},2} \leq M_{\text{ZAMS},1}$. In this model, the minimum mass of the secondary is equal to that of the primary ($5 M_{\odot}$) by construction.

- The mass ratio distribution by Stacy & Bromm (2013, hereafter SB13):

$$\xi(q) \propto q^{-0.55} \text{ with } q \in [0.1, 1] \text{ and } M_{\text{ZAMS},2} \geq 2.2 M_{\odot}. \quad (8)$$

This distribution was obtained from a fit to Pop. III stars formed in cosmological simulations (SB13).

2.2.3 Orbital period

We consider two different distributions for the orbital period (P):

- The distribution derived by S12 for O- and B-stars in the local Universe:

$$\xi(\pi) \propto \pi^{-0.55} \text{ with } \pi = \log(P/\text{day}) \in [0.15, 5.5]. \quad (9)$$

- A Gaussian distribution

$$\xi(\pi) \propto \exp\left[-(\pi - \mu)^2 / (2\sigma^2)\right] \quad (10)$$

with $\mu = 5.5$, and $\sigma = 0.85$, as derived from SB13 based on cosmological simulations. While this distribution is likely affected by the numerical resolution of the original simulations, which suppresses the formation of systems with short orbital periods, we decide to consider it as a robust upper limit to the orbital period of Pop. III binary stars.

2.2.4 Eccentricity

We compare two distributions for the orbital eccentricity (e):

- The distribution obtained by S12 and based on a sample of O- and B-type stars in the local Universe:

$$\xi(e) \propto e^{-0.42} \text{ with } e \in [0, 1). \quad (11)$$

- The thermal distribution, adopted for Pop. III binaries by, e.g., Kinugawa et al. (2014); Hartwig et al. (2016); Tanikawa et al. (2021b):

$$\xi(e) = 2e \text{ with } e \in [0, 1). \quad (12)$$

Table 1. Initial conditions.

Model	$M_{ZAMS,1}$	M_{ZAMS}	q	P	e
LOG1	Flat in log	–	S12	S12	S12
LOG2	Flat in log	–	S12	SB13	Thermal
LOG3	–	Flat in log	Sorted	S12	S12
LOG4	Flat in log	–	SB13	S12	Thermal
LOG5	Flat in log	–	SB13	SB13	Thermal
KRO1	K01	–	S12	S12	S12
KRO5	K01	–	SB13	SB13	Thermal
LAR1	L98	–	S12	S12	S12
LAR5	L98	–	SB13	SB13	Thermal
TOP1	Top heavy	–	S12	S12	S12
TOP5	Top heavy	–	SB13	SB13	Thermal

Column 1 reports the model name. Column 2 describes how we generate the ZAMS mass of the primary star (i.e., the most massive of the two members of the binary system). Column 3 describes how we generate the ZAMS mass of the overall stellar population (without differentiating between primary and secondary stars). We follow this procedure only for model LOG3 (see the text for details). Columns 4, 5, and 6 specify the distributions we used to generate the mass ratios q , the orbital periods P and the orbital eccentricity e . See Section 2.2 for a detailed description of these distributions.

2.2.5 Input catalogues

We build 11 different input catalogues by varying the aforementioned distributions of the IMF, q , P , and e . We set the total number of generated binaries to obtain 10^7 binaries in the high-mass regime ($M_{ZAMS,2} \geq 10 M_{\odot}$, and $M_{ZAMS,1} \geq 10 M_{\odot}$ by construction). This ensures a good sampling of the high-mass regime and reduces the stochastic fluctuations (e.g., Iorio et al. 2023). Table 1 lists the properties of our input catalogues. We refer to Costa et al. (2023) for more details.

2.3 Formation history of Pop. III stars

We consider four independent estimates of the Pop. III star formation rate density (SFRD), to quantify the main differences among models. Figure 1 shows these four star formation rate histories, which come from Hartwig et al. (2022, hereafter H22), Jaacks et al. (2019, hereafter J19), Liu & Bromm (2020b, hereafter LB20), and Skinner & Wise (2020, hereafter SW20). All of them are consistent with the value of the Thomson scattering optical depth estimated by the Planck Collaboration (i.e. $\tau_e = 0.0544 \pm 0.0073$, Ade et al. 2016).

The peak of the Pop. III SFRD is remarkably different in these four models, ranging from $z \approx 8$ (J19) to $z \approx 20$ (SW20). By selecting these four SFRDs, we account for differences in the underlying physics assumptions and for the cosmic variance, since these models rely on cosmological boxes with length spanning from 1 to $8 h^{-1}$ comoving Mpc. All of these SFRDs come from semi-analytic models or cosmological simulations that assume their own IMF for Pop. III stars. Thus, we introduce an inconsistency whenever we combine a given SFRD model with a binary population synthesis catalogue generated with a different IMF. We expect that the impact of this assumption on our results is negligible compared to other sources of uncertainty considered in this work (e.g., Crosby et al. 2013).

2.3.1 H22

A-SLOTH is the only semi-analytic model that samples and traces individual Pop. III and II stars, and is calibrated on several observables from the local and high-redshift Universe (Hartwig et al. 2022; Uysal & Hartwig 2023). It can take input dark-matter halo

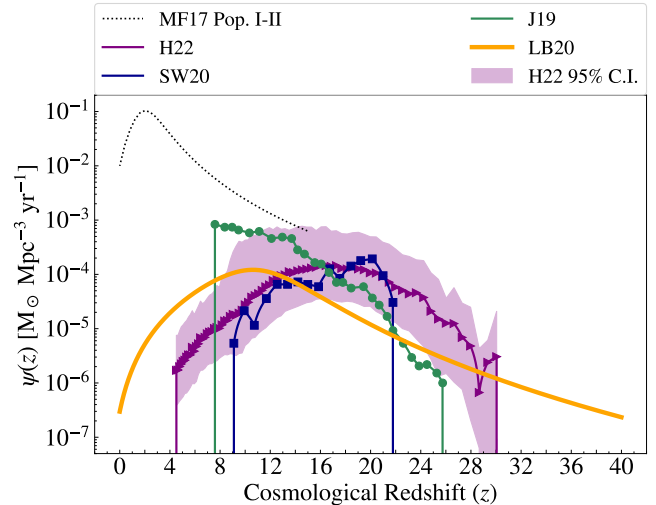


Figure 1. Star formation rate density $\psi(z)$ of Pop. III stars. Purple line: Hartwig et al. (2022) (H22); blue line: Skinner & Wise (2020) (SW20); green line: Jaacks et al. (2019) (J19); orange line Liu & Bromm (2020a) (LB20). The shaded area shows the 95% credible interval for the H22 model. The thin dotted black line is the star formation rate density of Pop. I-II stars from Madau & Fragos (2017) (MF17).

merger trees either from cosmological simulations or from an extended Press-Schechter formalism. Here, we use the results obtained with the merger tree from Ishiyama et al. (2016), who simulated a $(8 h^{-1} \text{ Mpc})^3$ box down to a redshift $z = 4$.

With A-SLOTH, it is possible to quantify the uncertainties in the SFRD that arise from unconstrained input parameters of the semi-analytic model (such as star formation efficiency or Pop. III IMF). Hartwig et al., in prep., characterise these uncertainties through a Monte-Carlo Markov Chain (MCMC) exploration. They calibrate A-SLOTH with a rejection sampler that should maximise the log likelihood, which is based on nine independent observables. After the initial burn-in phase, they record every accepted model. In this way, they explore the parameter space around the optimum and obtain various different models that all reproduce observables equally well. The MCMC runs provide > 5000 accepted models, each with a slightly different SFRD. From these models, we have extracted the central 95% credible interval of the SFRD. Figure 1 shows this 95% credible interval, which reflects uncertainties in the unconstrained input parameters.

2.3.2 J19

Jaacks et al. (2019) used the hydro-dynamical/ N -body code GIZMO (Hopkins 2015) coupled with custom sub-grid physics, accounting for both the chemical and radiative feedback from core-collapse and pair-instability supernovae. The simulation has been run down to $z = 7.5$ with a comoving box length of $4 h^{-1}$ Mpc.

2.3.3 LB20

Liu & Bromm (2020b) also ran a cosmological simulation with GIZMO, but assumed different sub-grid prescriptions, resulting in a lower Pop. III SFRD compared to Jaacks et al. (2019). They simulated a comoving cubic box of $(4 h^{-1} \text{ Mpc})^3$ down to redshift $z = 4$, and then extrapolate the results to $z = 0$ with additional semi-analytic

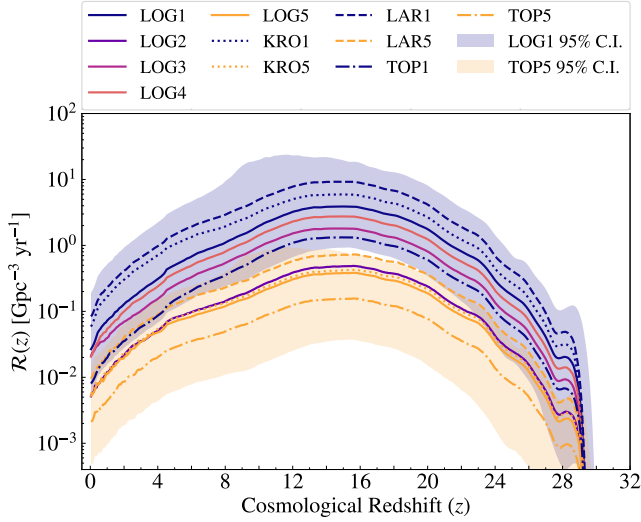


Figure 2. Evolution of the BBH merger rate density with redshift $\mathcal{R}(z)$ assuming the SFRD from H22, and the corresponding 95% credible interval. Solid lines: models with a flat-in-log IMF (LOG). Dotted lines: Kroupa IMF (KRO). Dashed lines: Larson IMF (LAR). Dot-dashed lines: top-heavy IMF (TOP). The shaded areas are 95% credible interval evaluated considering input uncertainty in Λ -SLOTH (see Figure 1 and Section 2.3.1) for the models LOG1 and TOP5.

modelling. They parameterised their Pop. III SFRD evolution with the same functional form as Madau & Dickinson (2014)

$$\psi(z) = \frac{a(1+z)^b}{1 + [(1+z)/c]^d} [\text{M}_\odot \text{yr}^{-1} \text{Mpc}^{-3}], \quad (13)$$

and obtained best-fit parameters $a = 756.7 \text{ M}_\odot \text{yr}^{-1} \text{Mpc}^{-3}$, $b = -5.92$, $c = 12.83$, and $d = -8.55$ (Liu & Bromm 2020b). In our analysis, we use this best fit.

2.3.4 SW20

Skinner & Wise (2020) ran a hydro-dynamical cosmological simulation with the adaptive mesh refinement code ENZO (Bryan et al. 2014). They simulate a $(1 h^{-1} \text{Mpc})^3$ comoving box with a 256^3 base grid resolution and a dark-matter particle mass of 2001 M_\odot . This simulation has been run down to $z = 9.32$.

2.4 COSMORATE

We estimate the merger rate density evolution of BBHs with the semi-analytic code COSMORATE (Santoliquido et al. 2020, 2021), which interfaces catalogues of simulated BBH mergers with a metallicity-dependent SFRD model. The merger rate density in the comoving frame is given by

$$\mathcal{R}(z) = \int_{z_{\max}}^z \left[\int_{Z_{\min}}^{Z_{\max}} \mathcal{S}(z', Z) \mathcal{F}(z', z, Z) dZ \right] \frac{dt(z')}{dz'} dz', \quad (14)$$

where $\mathcal{S}(z', Z) = \psi(z') p(z', Z)$. Here, $\psi(z')$ is the adopted star formation rate density evolution (chosen among the ones presented in Figure 1), and $p(z', Z)$ is the distribution of metallicity Z at fixed formation redshift z' . Since we model Pop. III stars with a single metallicity ($Z = 10^{-11}$), we define $p(z', Z)$ as a delta function for Pop. III stars, different from zero only if $Z = 10^{-11}$. In Equation 14, $dt(z')/dz' = H_0^{-1} (1+z')^{-1} [(1+z')^3 \Omega_M + \Omega_\Lambda]^{-1/2}$, where

H_0 is the Hubble parameter, Ω_M and Ω_Λ are the matter and energy density, respectively. We adopt the values of Aghanim et al. (2020). The term $\mathcal{F}(z', z, Z)$ in Equation 14 is given by:

$$\mathcal{F}(z', z, Z) = \frac{1}{\mathcal{M}_{\text{TOT}}(Z)} \frac{d\mathcal{N}(z', z, Z)}{dt(z)}, \quad (15)$$

where $\mathcal{M}_{\text{TOT}}(Z)$ is the total simulated initial stellar mass in our binary population-synthesis simulations, and $d\mathcal{N}(z', z, Z)/dt(z)$ is the rate of BBHs that form from progenitor metallicity Z at redshift z' and merge at z , extracted from our population-synthesis catalogues.

For all the Pop. III models shown in this work, we assume that the binary fraction is $f_{\text{bin}} = 1$, and we do not apply any correction for not sampling stars with mass $< 5 \text{ M}_\odot$. We make this simplifying assumption because we do not know the minimum mass and binary fraction of Pop. III stars. Assuming a lower binary fraction and a lower minimum mass than $m_{\text{min}} = 5 \text{ M}_\odot$ translates into a shift of our merger rate by a constant numerical factor (unless we assume that the minimum mass and the binary fraction depend on either redshift or metallicity).

2.5 Einstein Telescope detection rate

We evaluate the detection rate of Pop. III BBH mergers (\mathcal{R}_{det}) by the Einstein Telescope, as follows (e.g., Fishbach et al. 2021; Broekgaarden et al. 2022):

$$\mathcal{R}_{\text{det}} = \int \frac{d^2 \mathcal{R}(m_1, m_2, z)}{dm_1 dm_2} \frac{1}{(1+z)} \frac{dV_c}{dz} p_{\text{det}}(m_1, m_2, z) dm_1 dm_2 dz, \quad (16)$$

where the distribution of merger rate density as a function of primary m_1 and secondary mass m_2 is given by

$$\frac{d^2 \mathcal{R}(m_1, m_2, z)}{dm_1 dm_2} = \mathcal{R}(z) p(m_1, m_2 | z). \quad (17)$$

In Equation 17, $\mathcal{R}(z)$ is the merger rate density as a function of redshift (in units of $\text{Gpc}^{-3} \text{yr}^{-1}$, Equation 14) and $p(m_1, m_2 | z)$ is the two-dimensional source-frame mass distribution at a given redshift extracted with COSMORATE for each astrophysical model (Table 1). The factor $1/(1+z)$ converts source-frame time to detector-frame time and dV_c/dz is the differential comoving volume element.

In Equation 16, $p_{\text{det}}(m_1, m_2, z)$ is the probability of detecting a single system with parameters m_1 , m_2 , and z . We assume that $p_{\text{det}}(m_1, m_2, z)$ is an Heaviside step function, i.e. $p_{\text{det}}(m_1, m_2, z) = 1$ only if $\rho > \rho_{\text{th}}$, where ρ is the total signal-to-noise ratio (SNR) and $\rho_{\text{th}} = 9$. To evaluate the total SNR, we assume that the Einstein Telescope is composed of three independent, identical, and triangular-shaped detectors. Therefore, we evaluate the total SNR as (e.g., Singh & Bulik 2021; Yi et al. 2022):

$$\rho = \rho_{\text{opt}} \sqrt{\omega_0^2 + \omega_1^2 + \omega_2^2} \quad (18)$$

where ρ_{opt} is the optimal SNR (Finn & Chernoff 1993; Dominik et al. 2015; Taylor & Gerosa 2018; Bouffanais et al. 2019; Chen et al. 2021):

$$\rho_{\text{opt}}^2 = 4 \int_{f_{\text{low}}}^{f_{\text{high}}} df \frac{|\tilde{h}(f)|^2}{S_n(f)} \quad (19)$$

with $f_{\text{low}} = 2 \text{ Hz}$ and $f_{\text{high}} = 1000 \text{ Hz}$. The frequency domain response of ET ($\tilde{h}(f)$) to a face-on non-precessing BBH merger signal with m_1 , m_2 and z is generated using PYCBC (Biver et al. 2019) and assuming IMRPHENOMXAS as the phenomenological waveform model (García-Quirós et al. 2020). In Equation 19, $\omega_i = \Theta_i/4$ where

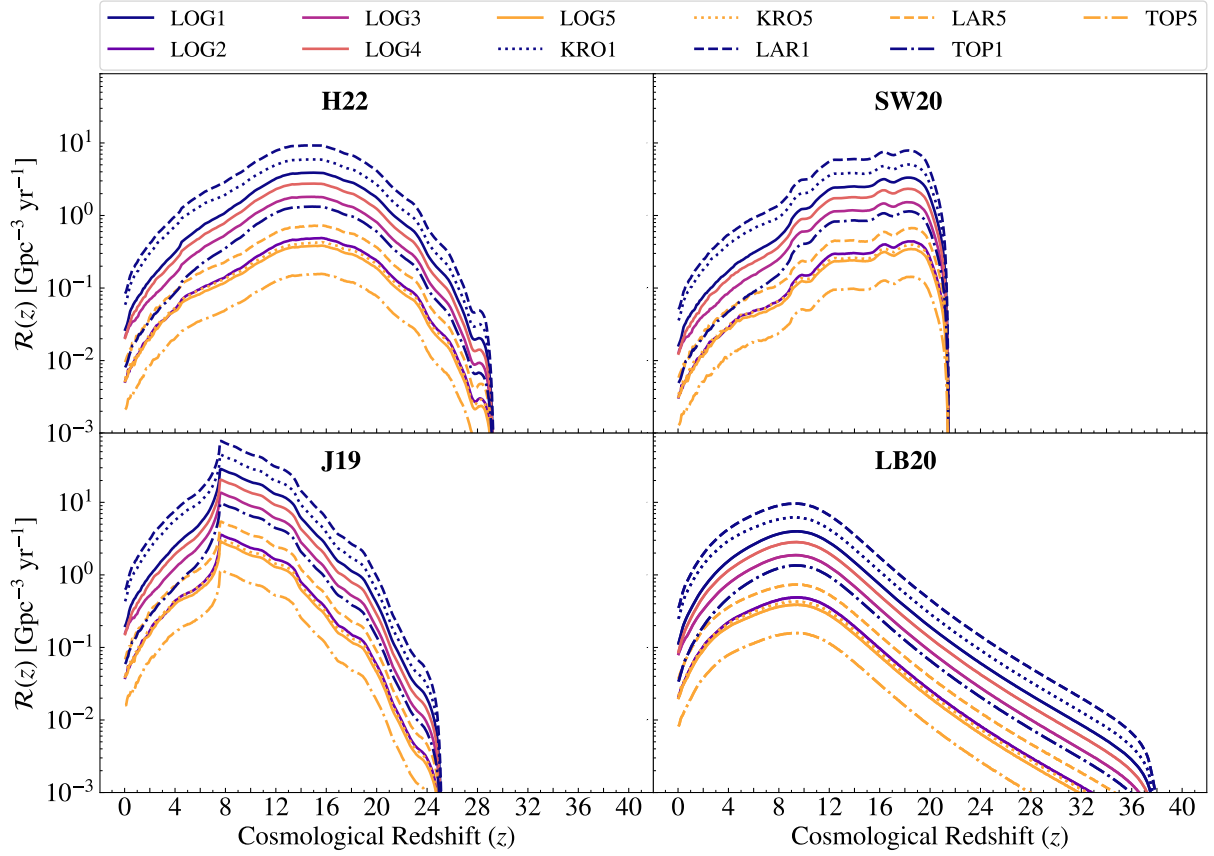


Figure 3. Evolution of the BBH merger rate density with redshift $\mathcal{R}(z)$ for all the 44 models considered in this work. Solid lines: models with a flat-in-log IMF (LOG). Dotted lines: Kroupa IMF (KRO). Dashed lines: Larson IMF (LAR). Dot-dashed lines: top-heavy IMF (TOP). Upper left plot: **H22** star formation history, upper right: **SW20**, lower left: **J19**, and lower right: **LB20**.

$i = 0, 1, 2$ is the index of the interferometer and Θ_i is the angular dependence of the GW signal, defined as:

$$\Theta_i = 2[F_{+,i}^2(1 + \cos^2 \iota)^2 + 4F_{\times,i}^2 \cos^2 \iota]^{1/2} \quad (20)$$

with $0 < \Theta_i < 4$ (Finn & Chernoff 1993; Singh & Bulik 2021) and $\cos \iota$ is the cosine of the inclination angle randomly sampled in the range $[-1, 1]$. The Einstein Telescope will have three nested interferometers, rotated by 60° with respect to each other (Regimbau et al. 2012). The antenna pattern for each interferometer is thus $F_{+,i}(\theta, \phi, \psi) = F_{+,0}(\theta, \phi + 2i\pi/3, \psi)$ and $F_{\times,i}(\theta, \phi, \psi) = F_{\times,0}(\theta, \phi + 2i\pi/3, \psi)$, where θ, ϕ denote the sky position and ψ is the polarisation angle. The response function $F_{+,0}$ and $F_{\times,0}$ are given as (Finn & Chernoff 1993; Regimbau et al. 2012; Singh & Bulik 2021):

$$F_{+,0} = \frac{\sqrt{3}}{4}(1 + \cos^2 \theta) \cos 2\phi \cos 2\psi - \frac{\sqrt{3}}{2} \cos \theta \sin 2\phi \sin 2\psi \quad (21)$$

and

$$F_{\times,0} = \frac{\sqrt{3}}{4}(1 + \cos^2 \theta) \cos 2\phi \sin 2\psi + \frac{\sqrt{3}}{2} \cos \theta \sin 2\phi \cos 2\psi. \quad (22)$$

We assume all the sources to be isotropically distributed, therefore we randomly sample $\cos \theta$, ϕ , and ψ in the ranges $[-1, 1]$, $[-\pi, \pi]$, and $[-\pi, \pi]$, respectively. In Equation 19, $S_n(f)$ is the noise power spectral density and represents the sensitivity of the detector to GWs

at different frequencies. In our calculation, we adopt the ET-D 10-km triangle configuration for $S_n(f)$ ¹ (Hild et al. 2008, 2010, 2011).

3 RESULTS

3.1 Merger rate density of BBHs born from Pop. III stars

Figure 2 shows the merger rate density evolution of Pop. III BBHs assuming the SFRD from **H22**. The merger rate density changes by about one order of magnitude within the 95% credible interval of the Pop. III SFRD estimated by **H22**. Uncertainties on the initial conditions of binary systems (Table 1) impact the merger rate density of Pop. III BBHs by up to two orders of magnitude, for a fixed SFRD model. The models adopting a **SB13** distribution for the initial orbital periods (LOG2, LOG5, KRO5, LAR5, and TOP5) have lower merger rate densities than models adopting the distribution by **S12** (all the remaining models). The reason is that short orbital periods, as in the case of **S12**, favour the merger of BBHs via stable mass transfer episodes between the progenitor stars.

Figure 3 shows the merger rate density for all the SFRD models considered in this work. The star formation rate history affects both the shape and the normalisation of the BBH merger rate density. Our merger rate density curves (Fig. 3) are similar in shape to the SFRD

¹ ET sensitivity curves are available at <https://www.et-gw.eu/index.php/etsensitivities>

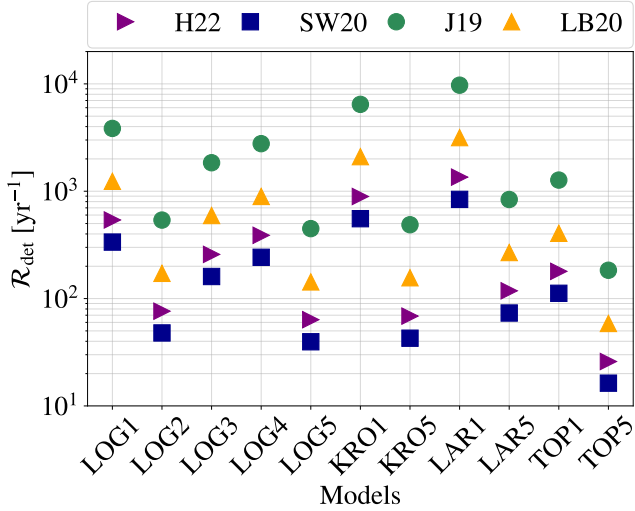


Figure 4. Detection rate \mathcal{R}_{det} of Pop. III BBHs, assuming the Einstein Telescope triangle configuration (ET-D) and $\rho_{\text{th}} = 9$. See Section 2.5 for details. Purple right-pointing triangles: SFRD from H22; blue squares: SW20; green circles: J19; orange triangles: LB20.

curves (Fig. 1), with just a shift to lower redshift because of the delay time, i.e. the time between the formation of a BBH-progenitor binary system and the merger of the two BHs. Hence, the peak of the merger rate density spans from $z \approx 16$ to $z \approx 8$ depending on the SFRD model. For all the considered star formation rate histories and binary models, the BBH merger rate density peaks well inside the instrumental horizon of the Einstein Telescope (Maggiore et al. 2020; Kalogera et al. 2021).

3.2 Detection rate of Pop. III BBHs with the Einstein Telescope

We have estimated the detection rate of Pop. III BBH mergers that we expect to obtain with the Einstein Telescope, in the 10-km triangle configuration (ET-D, Hild et al. 2008, 2010, 2011), as described in Section 2.5. Figure 4 shows the detection rate for all our models. Overall, we expect that the Einstein Telescope will detect between 10 and 10^4 BBH mergers from Pop. III stars in one year of observation. The highest predicted rates ($\mathcal{R}_{\text{det}} > 10^3 \text{ yr}^{-1}$) are associated with the SFRD from J19 and with the initial orbital period distribution from S12. These numbers refer to mergers that happen inside the Einstein Telescope instrumental horizon, without distinguishing between high- and low-redshift mergers.

We expect that a large fraction of the detected Pop. III BBH mergers occur at redshift $z > 8$, during or before the cosmic reionization. This value significantly depends on the adopted SFRD model: we estimate that 60–71% detectable Pop. III BBH mergers take place at $z > 8$ according to H22, 66–78% according to SW20, 45–54% with the SFRD by J19, and 28–34% assuming LB20. These high-redshift detections are particularly important, because they will allow us to characterize the properties of Pop. III BBHs.

3.3 Evolution of BH mass with redshift

Figure 5 shows that the median value of the primary BH mass (i.e., the most massive between the two merging BHs) does not change significantly with redshift, considering the entire ensemble of our models. On the other hand, the median mass of the secondary BH

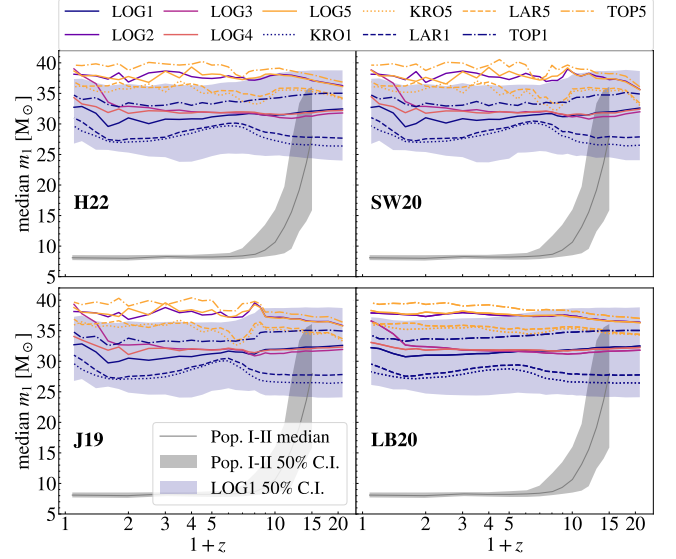


Figure 5. Median primary BH mass m_1 as a function of redshift, for all the models considered in this work. The blue shaded area is the interval from the 25th to the 75th percentile of the primary BH mass distribution at fixed redshift for the LOG1 model. Upper left-hand panel: H22 SFRD model, upper right-hand panel: SW20, lower left-hand panel: J19, and lower right-hand panel: LB20. The grey thin solid line shows the median primary mass of Pop. I-II BBHs in our fiducial model (Appendix A). The shaded grey area is the corresponding 50% credible interval.

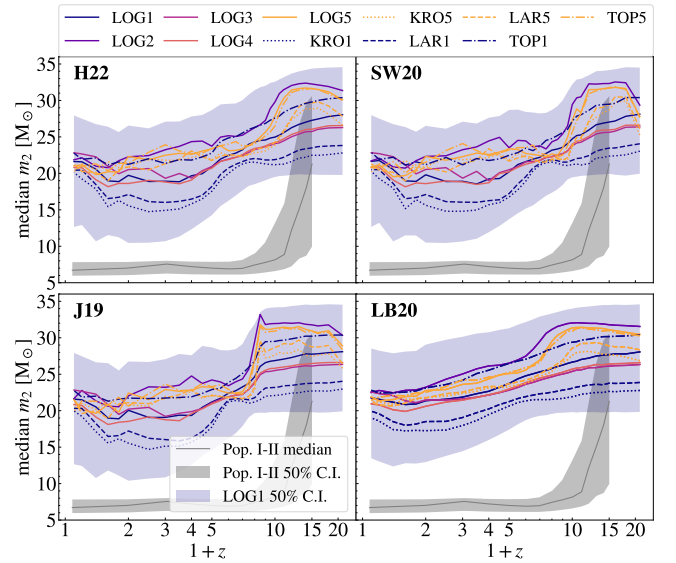


Figure 6. Same as Figure 5 but for the secondary BH mass m_2 .

mass does decrease at lower redshift (Figure 6). This trend of the secondary BH mass is more evident when the SFRD of Pop. III becomes negligible.

As a consequence, the mass ratio of Pop. III BBHs (Figure 7) decreases from $q \gtrsim 0.9$ at $z \sim 15$ to $q \sim 0.5 - 0.7$ at $z \leq 4$. In contrast, the mass ratio of Pop. I-II BBHs (Appendix A) remains nearly constant $q \gtrsim 0.9$ across all redshifts.

Figures 8 and 9 show the whole distribution of primary and sec-

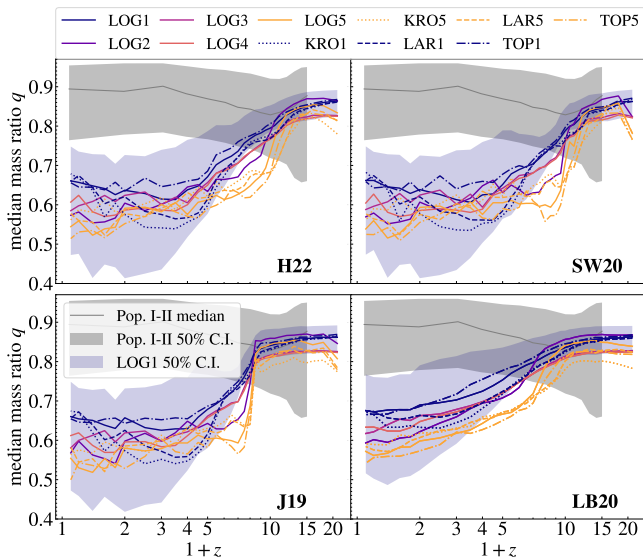


Figure 7. Same as Figure 5 but for the BH mass ratio q .

ondary masses of Pop. III BHs, respectively, at redshift $z = 0, 2,$ and 10 . The percentage of Pop. III BBHs with $m_2 \geq 25 M_\odot$ is $\sim 60 - 80\%$ at $z = 10$ and only $\sim 25 - 40\%$ at $z = 0$ (depending on the chosen model). This change of the shape is a result of the different distribution of delay times. In fact, when the formation rate of Pop. III stars becomes negligible, we expect to see only mergers of Pop. III BBHs with long delay times. We further discuss this feature in Section 4.1, considering the impact of the various formation channels.

Figures 5-9 also compare the behaviour of Pop. III BBHs with that of Pop. I-II BBHs (grey shaded area, modelled as described in Appendix A). Both the median primary and secondary BH mass of BBHs born from Pop. I-II stars decrease at redshift $z < 10$. This happens because at low redshift most BBH mergers have metal-rich progenitors, and the BH mass strongly depends on the assumed metallicity (Santoliquido et al. 2021, 2022).

At low redshift, our intermediate- and high-metallicity stars ($Z \geq 10^{-3}$) produce a main peak in the primary BH mass distribution at $8 - 10 M_\odot$, similar to the main peak inferred from the LIGO–Virgo–KAGRA (LVK) data (Abbott et al. 2019, 2021, 2023; Farah et al. 2023; Callister & Farr 2023). Instead, primary BHs born from Pop. III stars have a preference for a mass $m_1 \approx 30 - 35 M_\odot$, which is in the range of the secondary peak inferred from the LVK data (Abbott et al. 2019, 2021, 2023; Farah et al. 2023; Callister & Farr 2023). The secondary peak has usually been interpreted as a signature of the pair-instability mass gap, but recently this interpretation has been put into question because the lower edge of the gap should be at higher masses ($> 50 M_\odot$, e.g., Farmer et al. 2020; Costa et al. 2021; Woosley & Heger 2021; Vink et al. 2021; Farag et al. 2022). Our results indicate that the secondary peak at $\sim 35 M_\odot$ might rather be a signature of the progenitor’s metallicity: metal-poor and metal-free stars in tight binary systems tend to end their life as naked helium cores with a mass of $\sim 30 - 40 M_\odot$, favouring a sub-population of BBHs in this mass range (e.g., Mapelli et al. 2013; Kinugawa et al. 2014; Ziosi et al. 2014; Belczynski et al. 2016; Mapelli 2016; Iorio et al. 2023).

4 DISCUSSION

4.1 Formation channels

To better understand the behaviour of Pop. III BBHs, we divide our sample into the four formation channels we already discussed in Iorio et al. (2023). Channel I includes all the systems that undergo a stable mass transfer before the first BH formation, and later evolve through at least one common-envelope phase. Channel II comprises the systems that interact through at least one stable mass transfer episode, without common envelopes.

Channel III and IV both include systems that undergo at least one common-envelope before the formation of the first BH. The only difference between these two channels is that in channel III one of the two components of the binary system still retains a residual fraction of its H-rich envelope at the time of the first BH formation, while in channel IV both stars have already lost their H-rich envelope at the time of the first BH formation. These four channels do not encompass all possible formation pathways of BBHs, but only the most common channels in our models.

Figure 10 shows the percentage of Pop. III binary stars evolving through each of the four channels and resulting in BBH mergers at $z = 10$ (upper panel) and $z = 0.1$ (lower panel). Channel I, which is commonly believed to be the main formation pathway for BBH mergers (e.g., Tauris & van den Heuvel 2006; Neijssel et al. 2019; Belczynski et al. 2020; Mandel & Müller 2020; Broekgaarden et al. 2021), has marginal importance ($\leq 7\%$) for Pop. III BBHs, regardless of the chosen initial conditions. This happens because mass transfer tends to remain stable in the late evolutionary stages, when the system is composed of a BH and a companion star, given the low mass ratio between the donor star and the BH.

Channel II (stable mass transfer) is the dominant channel ($\geq 50\%$) for most of our initial conditions, with the exception of LOG2, LOG5, KRO5, LAR5, and TOP5, for which channel II represents only $1 - 2\%$ of all the mergers. The latter five models are the only ones in our sample adopting the SB13 distribution for the orbital periods, which are significantly longer than the S12 orbital periods. Indeed, the stable mass transfer channel favours high-mass binary stars that start with a short orbital separation ($\leq 10^3 R_\odot$) and undergo a stable mass transfer early in their main sequence or Hertzsprung-gap phase (e.g., Pavlovskii et al. 2017; van den Heuvel et al. 2017; Giacobbo et al. 2018; Neijssel et al. 2019; Mandel & Müller 2020; Marchant et al. 2021; Gallegos-Garcia et al. 2021). This predominance of the stable mass transfer in the case of Pop. III stars is in agreement with Kinugawa et al. (2016) and Inayoshi et al. (2017). The large orbital periods in SB13 suppress this channel, because they prevent the formation of binary systems with initial orbital separation $< 10^3 R_\odot$.

Channel III and IV are complementary to channel II: they contribute together to $\sim 9 - 47\%$ of the BBH mergers when channel II is the dominant one and to $> 90\%$ when channel II is suppressed, i.e. for models LOG2, LOG5, KRO5, LAR5, and TOP5. In the latter five cases, the initial orbital periods are sufficiently large that the two stars start mass transfer only when their radii are significantly expanded, i.e. in the red giant phase. Because of their convective envelope, such mass transfer becomes unstable and triggers one or more common envelopes.

Channel III has generally longer delay times than channel IV (Figure 11) because it takes place in systems with low initial mass ratios: the secondary star is generally less massive than the BH produced by the primary star and mass transfer episodes after the formation of the first BH do not shrink the orbit. The long delay times of channel III explain why it becomes more important at $z = 0.1$ with respect to the high redshift.

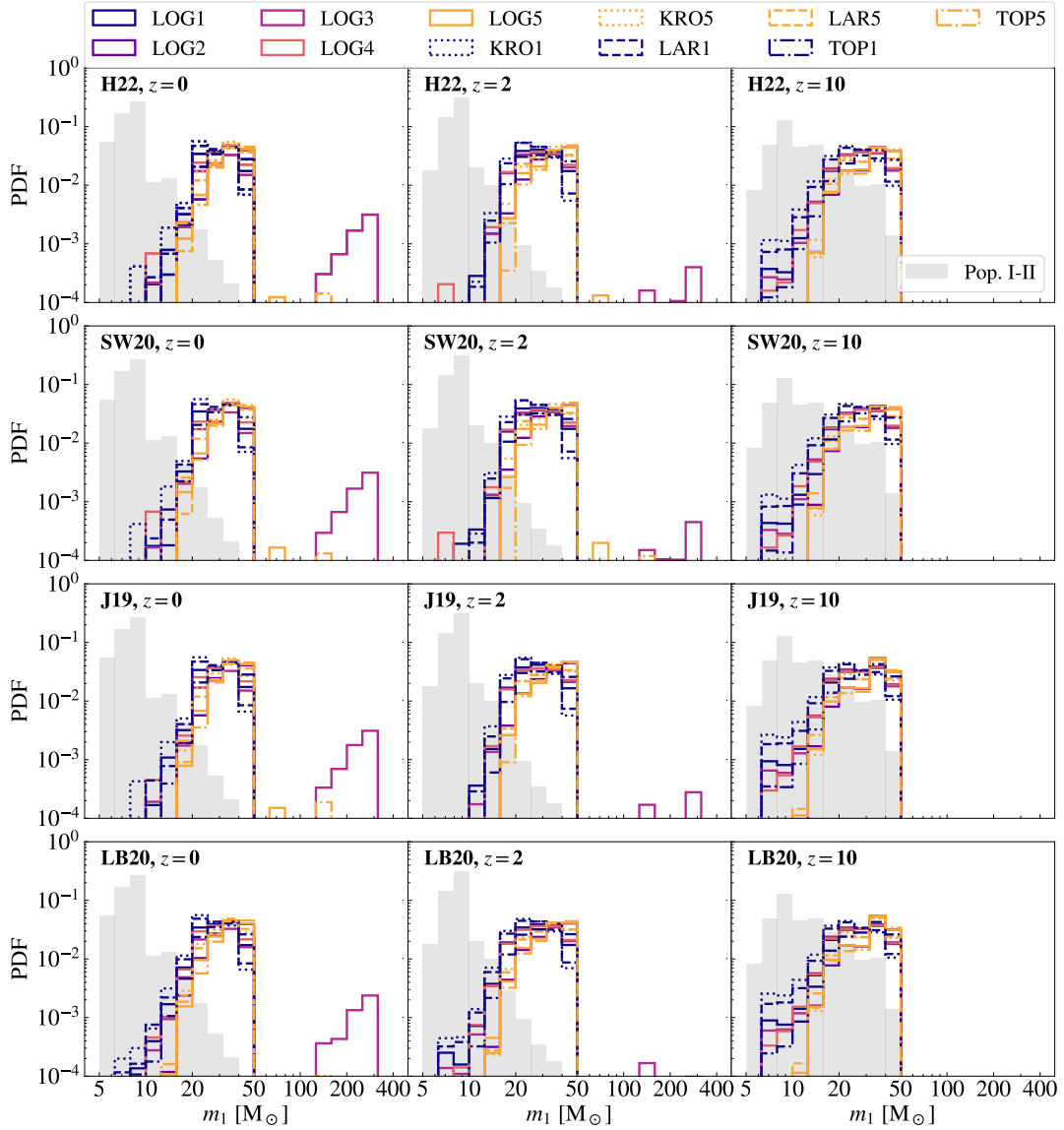


Figure 8. Primary BH mass distribution m_1 for three different redshift bins (from left to right $z = 0, 2$ and 10) and the four SFRD models considered in this work (from top to bottom **H22**, **SW20**, **J19** and **LB20**). The grey shaded histograms show the primary mass distribution of Pop. I-II BBHs in our fiducial model (Appendix A).

4.2 The evolution of the secondary mass

Our models calculated with the natal-kick distribution by **GM20** show that the median secondary mass of Pop. III BBH mergers in the local Universe is significantly lower than that of Pop. III BBHs in the early Universe. This leads to a sub-population of unequal-mass BBHs ($q \sim 0.1 - 0.7$), which might help us to identify Pop. III BBHs among the other LVK mergers, since most BBHs born from Pop. I–II stars are nearly equal mass in our simulations (**Santoliquido et al. 2021**; **Iorio et al. 2023**). Also, most LVK systems are nearly equal mass (**Abbott et al. 2023**).

Figures 11 and 12 show that this trend is an effect of delay time: the majority of the unequal mass BBHs (i.e., with low-mass secondary BHs) come from channel II and III. These Figures show that BBHs with low-mass secondary BHs have longer delay times in both channel II and III.

4.3 The effect of natal kicks

All the models we discussed so far adopt the natal kick model from **GM20**. This is our fiducial kick model because it naturally accounts for the claimed lower kicks in stripped and ultra-stripped supernovae (e.g., **Bray & Eldridge 2016**; **Tauris et al. 2017**; **Kruckow et al. 2018**; **Bray & Eldridge 2018**). On the other hand, the model by **GM20** has a major impact on the formation channels, because it introduces a dependence of the kick on the BH and ejecta mass.

Here, we consider an alternative model $\sigma 150$ (Section 2.1), in which the natal kicks have been randomly drawn from a Maxwellian distribution with parameter $\sigma = 150 \text{ km s}^{-1}$. In this alternative model, the natal kicks do not depend on the properties of the system. This implies that the $\sigma 150$ kicks are generally larger for stripped/ultra-stripped binaries and for high-mass BHs than the **GM20** kicks. This difference has a substantial impact on channel III.

Figure 11 shows the delay time distribution for four models: LOG1

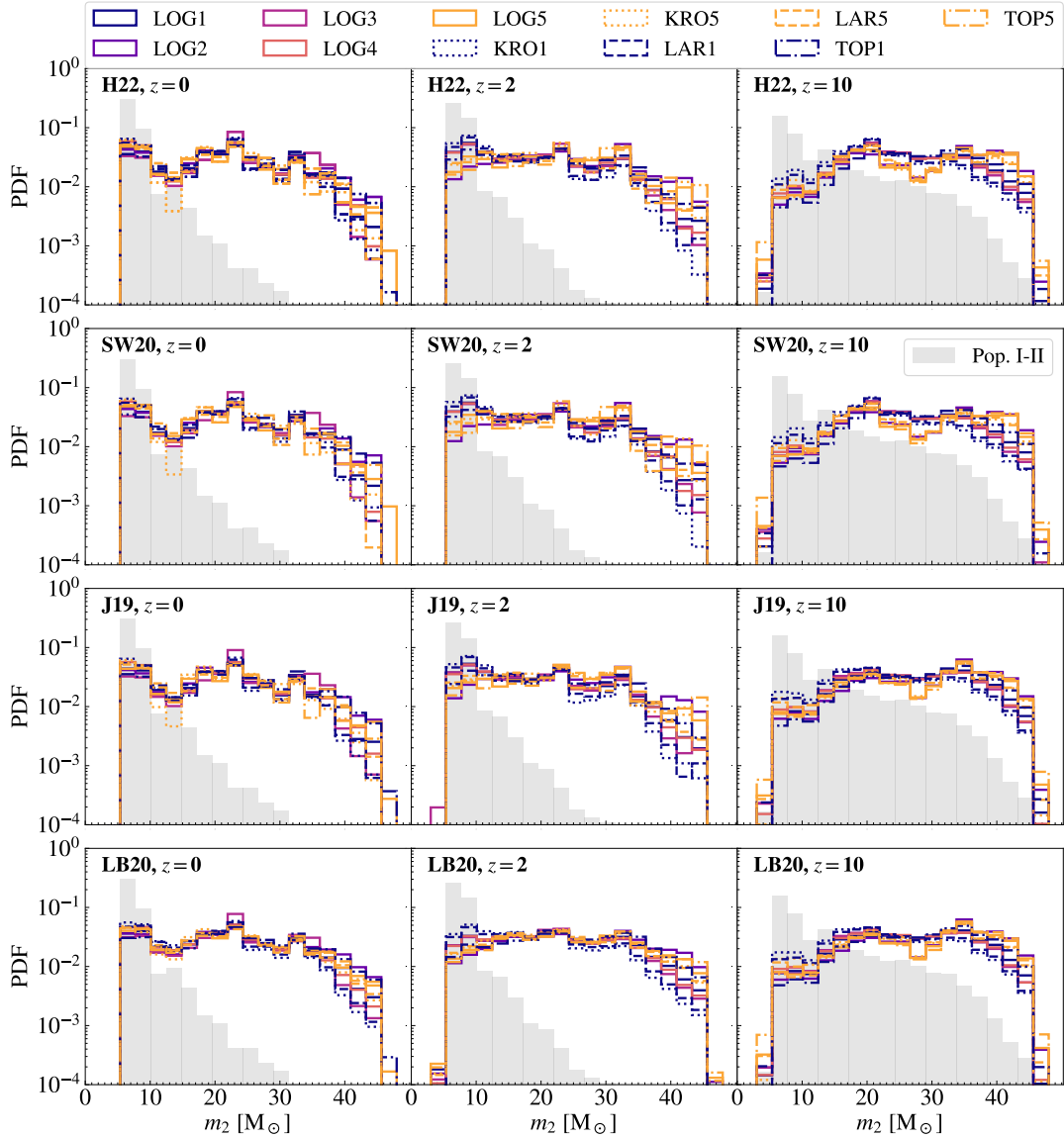


Figure 9. Same as Figure 8 but for the secondary BH mass m_2 .

and LAR5 adopt the kick distribution by GM20, while LOG1 σ 150 and LAR5 σ 150 adopt the σ 150 model. We distinguish the delay times of the four channels. The kick model barely affects channels II and IV, while it has a strong impact on channels I and III. Model σ 150 slightly increases the number of channel I BBH mergers, from nearly 0 to a few per cent. Most importantly, model σ 150 wildly changes the delay-time distribution of channel III mergers, populating the region of short delay times.

This difference springs from the impact of the natal kick on the orbital eccentricity. A larger kick either splits the binary, or increases its orbital eccentricity. Since the time of GW decay $t_{\text{GW}} \propto (1-e^2)^{7/2}$ (Peters 1964), a large eccentricity speeds up the BBH merger significantly. This effect is particularly important for channel III BBHs because they start from a large initial semi-major axis of the progenitor binary ($10^2 - 10^5 R_\odot$) and have lower secondary BH masses than the other channels (Costa et al. 2023).

The different delay time distribution of channel III has an obvious impact on the median mass of the secondary BH. Figure 13 shows

the evolution of the median secondary BH mass for models LOG1, LAR5, LOG1 σ 150, and LAR5 σ 150 (the same models as in Figure 11). The decrease of the median secondary BH mass with redshift almost completely disappears in the models with σ 150, because of the larger number of channel III mergers and of their different delay time distribution.

Still, the SN kick does not have a large impact on the merger rate density evolution of Pop. III BBHs, as shown in Fig. 14. The merger rate density of model LAR5 σ 150 is higher by a factor of two at the peak redshift ($z = 13$), where the variation of the number of channel III mergers is larger.

4.4 BBH mergers above and inside the mass gap

In our models of single Pop. III star evolution, the pair-instability mass gap extends from a BH mass $\approx 90 M_\odot$ to $\approx 240 M_\odot$, because we assume that the residual hydrogen envelope of the progenitor star is not ejected during core collapse (Figure 5 and Section 3.1 of Costa

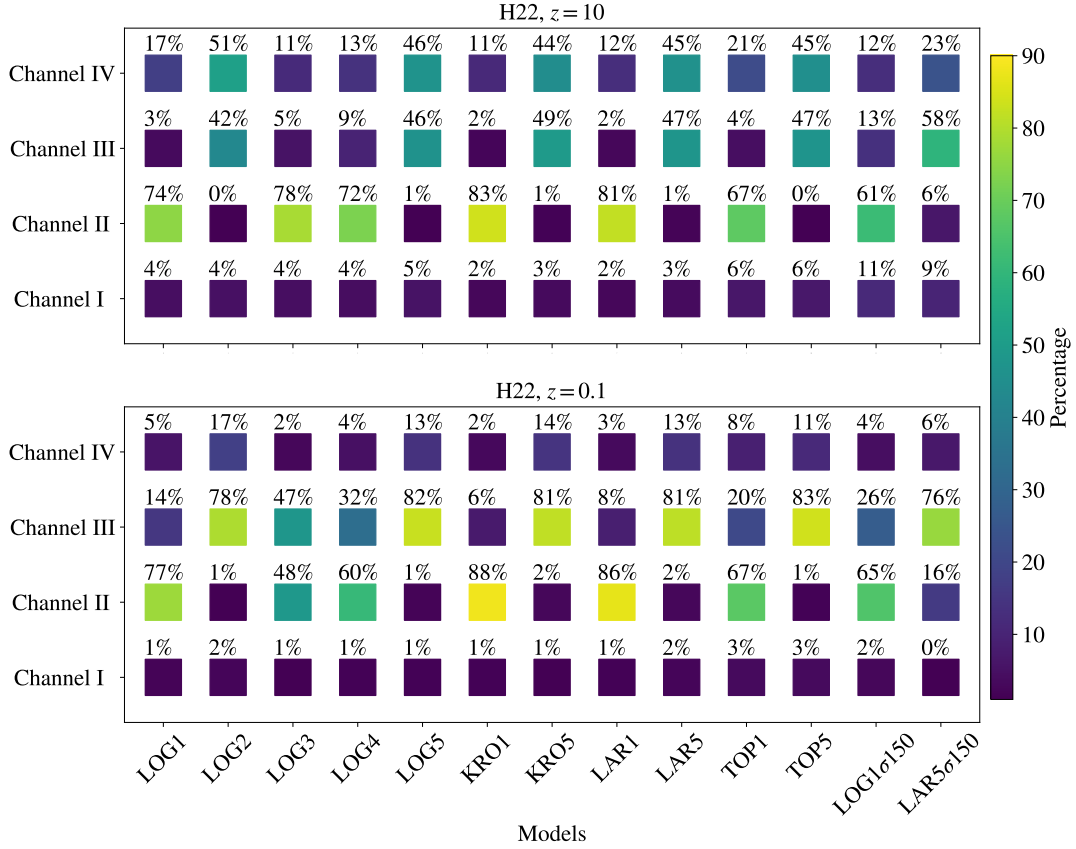


Figure 10. Percentage distribution of formation channels for all the models adopted in this work. Upper (lower) panel: Pop. III BBHs that merge at $z = 10$ ($z = 0.1$). Channel I includes all the systems that undergo a stable mass transfer before the first BH forms, and later evolve through at least one common-envelope phase. Channel II encompasses systems that interact only via stable mass transfer (no common envelopes). Channels III and IV consist in systems that experience at least one common envelope before the formation of the first BH. The only difference between them is that one of the two stars retains a fraction of its H-rich envelope until the formation of the first BH in channel III, while both stars have lost their envelope by the formation of the first BH in channel IV.

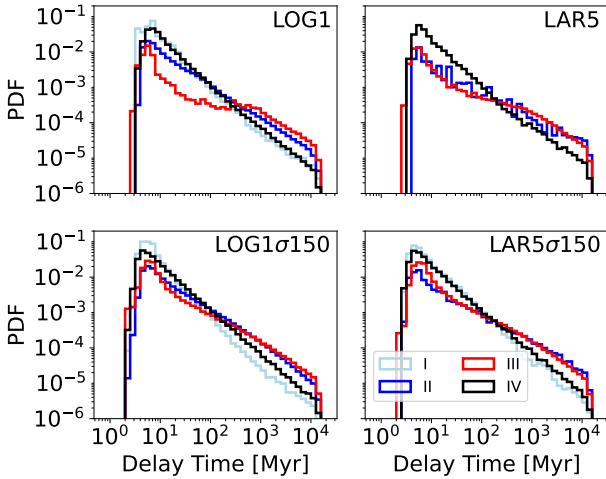


Figure 11. Distribution of delay times for models LOG1, LAR5, LOG1 σ 150 and LAR5 σ 150. Light-blue line: channel I; blue line: channel II; red line: channel III; black line: channel IV. Channel I is not shown in the case of LAR5 because of the low number of systems. These data come directly from the SEVN catalogues and are not convolved with redshift evolution.

et al. 2023). Instead, had we assumed that the hydrogen envelope is completely ejected, the pair instability mass gap would have shifted between a BH mass ≈ 50 and $\approx 130 M_{\odot}$, corresponding to the helium core mass at the boundaries of the gap.

Our models of binary star evolution allow the formation of BHs with mass both above and inside the pair-instability mass gap. In binary systems, mass accretion and stellar collisions possibly populate the mass gap, because they trigger the formation of stars with undersized He cores with respect to the hydrogen-rich envelope (Spera et al. 2019; Di Carlo et al. 2019; Renzo et al. 2020; Kremer et al. 2020; Tanikawa et al. 2021b; Banerjee 2022; Costa et al. 2022; Balone et al. 2023). However, in our Pop. III star simulations, BBH mergers with primary mass inside or above the gap are extremely rare.

Figure 15 shows that our Pop. III binary stars produce a very low merger rate density of BBHs with primary BH mass² $m_1 > 60 M_{\odot}$ in the Local Volume [$\mathcal{R}(m_1 > 60 M_{\odot}, z = 0) < 10^{-4} \text{ Gpc}^{-3} \text{ yr}^{-1}$], apart from the LOG3 model [$\mathcal{R}(m_1 > 60 M_{\odot}, z = 0) \approx 4 \times 10^{-3} \text{ Gpc}^{-3} \text{ yr}^{-1}$]. In our simulations, most BHs with mass inside or above the pair-instability gap are single objects or members

² In Figure 15, we consider $m_1 = 60 M_{\odot}$ as the lower edge of the pair-instability mass gap, because this is the most common value adopted in the literature (e.g., Abbott et al. 2020b), even if this value is lower than the one found in our models.

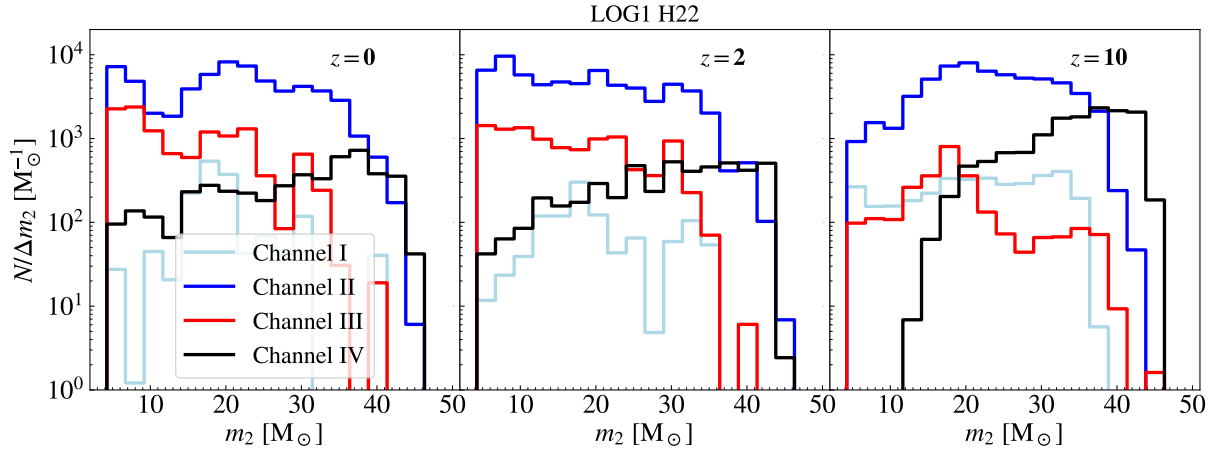


Figure 12. Secondary BH mass distribution m_2 for three different redshift bins (from left to right: $z = 0, 2$, and 10). We show model LOG1 with the H22 SFRD. Light-blue line: channel I; blue line: channel II; red line: channel III; black line: channel IV.

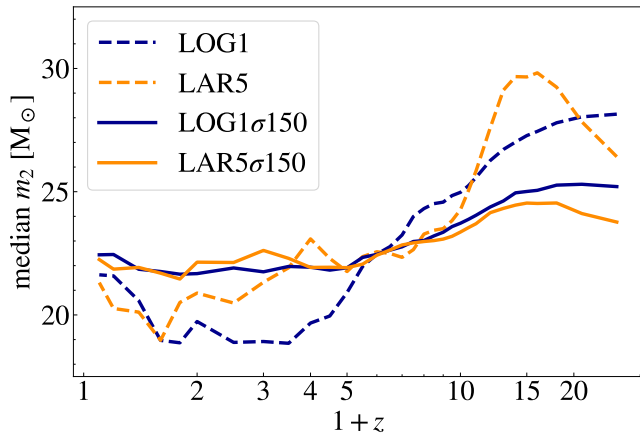


Figure 13. Evolution of the median secondary BH mass m_2 as a function of redshift, for LOG1 and LAR5, with the H22 star formation rate. Solid (dashed) line: natal kicks drawn from model σ 150 (GM20).

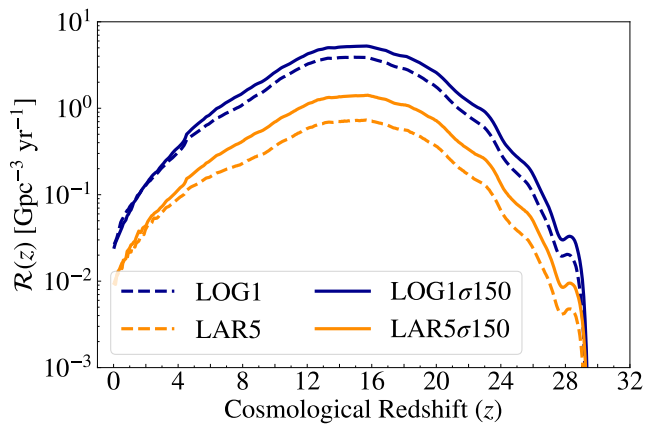


Figure 14. Evolution of the merger rate density with redshift $\mathcal{R}(z)$ for LOG1 and LAR5, with the H22 star formation rate. Solid (dashed) line: natal kicks from model σ 150 (GM20).

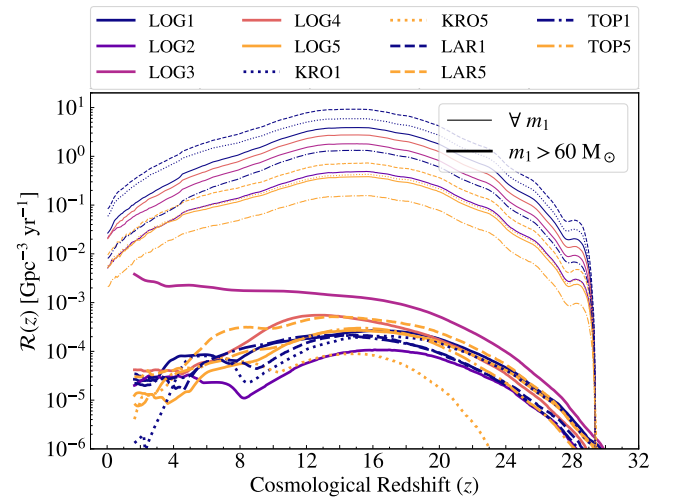


Figure 15. The thick lines show the merger rate density evolution of Pop. III BBHs with primary BH mass $m_1 > 60$ M $_{\odot}$. For comparison, the thin lines show the total merger rate density evolution of Pop. III BBHs (for any value of m_1). For all the models in this Figure, we use the Pop. III star SFRD from H22 (Figure 1). The colours and line types refer to different initial orbital parameters (Table 1).

of loose binary systems and do not merge within the lifetime of the Universe. Dynamical interactions in dense star clusters can dramatically boost the efficiency of BBH mergers inside and above the gap, because they favour dynamical exchanges and the hardening of massive binary systems (e.g., Di Carlo et al. 2020; Wang et al. 2022).

Furthermore, Figure 8 shows that we expect Pop. III BBH mergers with mass above the gap only at low redshift. The long delay times of channel III explain why we have BBH mergers with primary BH mass above the mass gap (> 120 M $_{\odot}$) only at low redshift in Figure 8, mainly in model LOG3. This model is the only one adopting a sorted distribution to pair up the progenitor stars. Hence, it is the one with the lowest initial mass ratios ($M_{ZAMS,2}/M_{ZAMS,1}$). Systems with $M_{ZAMS,1} \geq 250$ M $_{\odot}$ and initial semi-major axis $a_{\text{initial}} \in [10^3, 1.5 \times 10^5]$ R $_{\odot}$ evolve nearly unperturbed until the primary star becomes a giant star and fills its Roche lobe (Figure 16). In

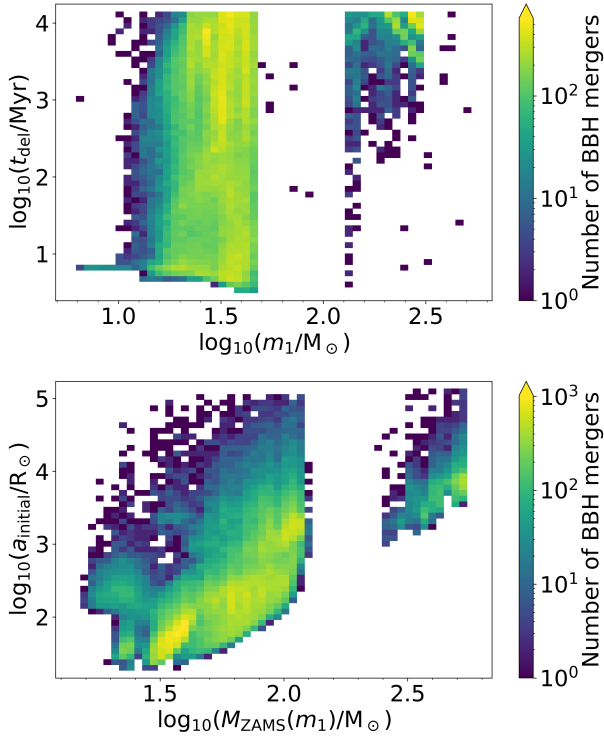


Figure 16. Properties of Pop. III BBH mergers and their progenitors in model LOG3. Upper panel: delay time t_{del} as a function of the primary BH mass m_1 . Lower panel: initial semi-major axis of the progenitor binary star a_{initial} versus ZAMS mass of the progenitor of the primary BH $M_{\text{ZAMS}}(m_1)$. These data come directly from the `SEVN` catalogues and are not convolved with redshift evolution.

channel III, the Roche lobe overflow becomes unstable and triggers a common envelope which removes the H-rich envelope of the primary star. Shortly after the common envelope phase, the primary star collapses to a BH above the pair-instability mass gap. Then, the binary evolves nearly unperturbed until the secondary star also becomes a BH. Given the large semi-major axis at the time of formation of the secondary BH ($\approx 100 R_{\odot}$) and the relatively low mass of the secondary BH ($m_2 \sim 10 - 30 M_{\odot}$), such binaries have a long delay time, of the order of 5 – 12 Gyr (Figure 16).

4.5 Comparison with previous work

We do not find any BBH mergers with primary mass in the $\sim 100 - 200 M_{\odot}$ regime, whereas Tanikawa et al. (2022b) find this sub-population of mergers in their fiducial model. This is mainly an effect of the different stellar radii. Tanikawa et al. (2022b) produce this sub-population of BBH mergers from binary stars with primary ZAMS mass $\sim 65 - 90 M_{\odot}$. In their fiducial model, such stars have radii $R < 100 R_{\odot}$ for their entire life, while in our models they expand much more during the end of the main sequence and the red giant phase (Costa et al. 2023). This comes from the choice of core overshooting: we assume an overshooting parameter $\Lambda_{\text{ov}} = 0.5$ in units of pressure scale height, which corresponds to $f_{\text{ov}} = 0.025$ in the formalism adopted by Tanikawa et al. (2022b), while they assume $f_{\text{ov}} = 0.01$ in the fiducial model (M-model). Indeed, our models are similar to the L-std model by Tanikawa et al. (2022b),

with $f_{\text{ov}} = 0.03$, and in this model they find no mergers with primary BH mass inside the mass gap (Fig. 6 of Tanikawa et al. 2022b).

The merger rate density of Pop. III BBHs estimated by Tanikawa et al. (2022b) reaches a maximum of $R(z \sim 10) \approx 20 \text{ Gpc}^{-3} \text{ yr}^{-1}$. In terms of the initial orbital parameters, their model is almost identical to our LOG1 model. They use the SFRD from SW20. In our LOG1 model with the SW20 SFRD, the merger rate peaks at $z \sim 16$ and $R(z \sim 16) \approx 2 \text{ Gpc}^{-3} \text{ yr}^{-1}$. The difference in the redshift of the peak is a consequence of the delay time distribution. Tanikawa et al. (2022b) have significantly longer delay times, even for their L-std model (see Figure 3 from Tanikawa et al. 2021a). The large difference in the normalisation of the peak between our work and Tanikawa et al. (2022b) is a consequence of the differences in our stellar and binary evolution models. In particular, our larger stellar radii increase the chance that two possible progenitor stars collide leaving just one single star, before they become a BBH.

4.6 A proxy for chemically homogeneous evolution (CHE)

We have adopted models of non-spinning Pop. III stars (Costa et al. 2023). Pop. III stars might be fast spinning (Yoon et al. 2012; Choplin et al. 2019). According to Tanikawa et al. (2021b), we can have a glimpse at what happens to fast-spinning stars by considering the evolution of pure-helium stars. In fact, fast spinning stars at low-metallicity effectively evolve toward chemically homogeneous evolution (CHE, de Mink & Mandel 2016; Mandel & de Mink 2016; Marchant et al. 2016; du Buisson et al. 2020; Riley et al. 2021). In this discussion, we use pure-He stars as a simplified proxy for CHE, which we will model carefully in future work.

Figure 17 shows that BBHs born from Pop. III pure-helium stars are crucially different from the other models presented here. Since pure-helium stars evolve with small radii ($< 100 R_{\odot}$), the most massive progenitor stars do not merge in the early stages of their life and efficiently produce BBH mergers above the mass gap. In the case of model LOG1, the merger rate density of Pop. III BBHs born from pure-He stars (Fig. 18) is higher than that of Pop. III BBHs born from H-rich stars. Moreover, the merger rate density of BBHs with primary mass $m_1 > 60 M_{\odot}$ is at least three orders of magnitude higher for pure-He star progenitors.

If we simulate pure-helium progenitors, we obtain similar results, i.e. a higher merger rate density and a larger population of BBHs above the gap, for all the modes assuming the S12 initial orbital periods (i.e. LOG1, LOG3, LOG4, KRO1, LAR1, and TOP1). In contrast, the merger rate density of models LOG2, LOG5, KRO5, LAR5, and TOP5 drops by at least two orders of magnitude in the case of pure-helium progenitors. The reason is that these models adopt the orbital period distribution from SB13, which suppresses short orbital separations. Since pure-helium stars are compact throughout their entire life, most of them do not undergo Roche-lobe overflow during their life and their orbital separations remain too large to merge within the lifetime of the Universe.

4.7 Pop. III BHs versus primordial BHs

The merger rate density of primordial BHs is predicted to scale as (e.g., De Luca et al. 2020; Mukherjee & Silk 2021; Mukherjee & Dizgah 2022; Mukherjee et al. 2022; De Luca 2022; Ng et al. 2022b; Franciolini et al. 2022)

$$\mathcal{R}_{\text{PBH}}(z) = \mathcal{R}_{\text{PBH}}(0) \left(\frac{t_{\text{age}}(z)}{t_{\text{age}}(0)} \right)^{-34/37}, \quad (23)$$

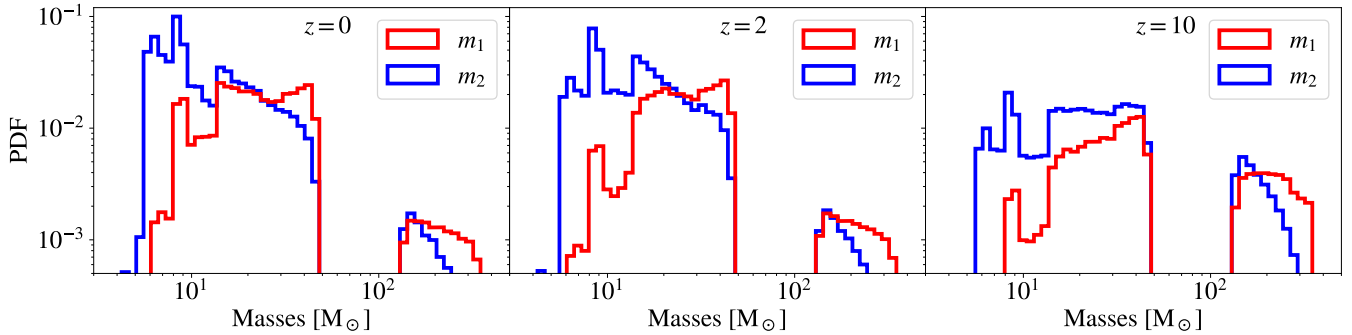


Figure 17. Primary BH mass (red) and secondary BH mass (blue) of Pop. III BBHs merging at redshift $z = 0$, (left), 2 (middle), and 10 (right) assuming the star formation history from H22 and the initial binary orbital parameters as in model LOG1 (Table 1). Here, we evolve pure-helium stars.

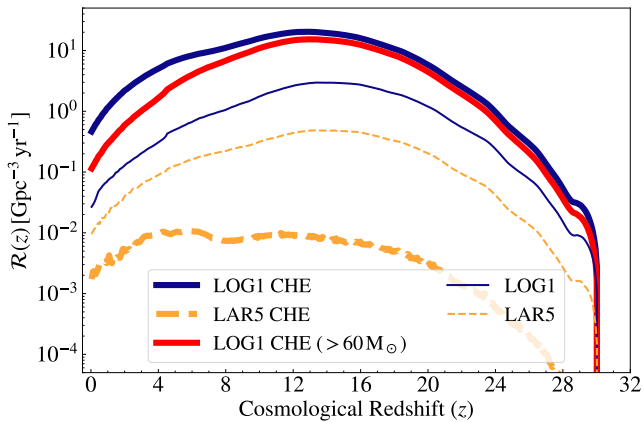


Figure 18. Merger rate density of Pop. III BBHs born from pure-helium binary stars assuming the star formation history from H22. Thick solid blue line: pure-helium binary stars evolved with LOG1 initial conditions. Thick solid red line: we show only the merger rate density of BBHs with primary mass $> 60 M_{\odot}$ for pure-helium binary stars evolved with LOG1 initial conditions. Thick dashed orange line: pure-helium binary stars evolved with LAR5 initial conditions. Thin solid blue (Thin dashed orange) line: model LOG1 (LAR5) with pure-hydrogen binary stars for comparison.

where $t_{\text{age}}(z)$ is the age of the Universe at redshift z . According to Franciolini et al. (2022), current LVK data suggest that $\mathcal{R}_{\text{PBH}}(0) \leq 5.3 \text{ Gpc}^{-3} \text{ yr}^{-1}$ at 90% credible interval, if we assume primordial BH masses $\geq 3 M_{\odot}$. This implies that our predicted merger rate density of Pop. III BBHs is always below the upper bound of the merger rate density of primordial BHs, even for the J19 model at $z \approx 8$, for which we have $\mathcal{R}(z=8) \leq 80 \text{ Gpc}^{-3} \text{ yr}^{-1}$ (Fig. 3) versus $\mathcal{R}_{\text{PBH}}(z=8) \leq 90 \text{ Gpc}^{-3} \text{ yr}^{-1}$.

If we assume that primordial BHs represent a fraction 10^{-4} of the total dark matter energy density (e.g., Fig. 3 from Ng et al. 2022b), then we expect that Pop. III BBH mergers outnumber primordial BH mergers out to redshift $z \sim 15 - 20$ in our most optimistic models. Overall, the slope of the merger rate density of primordial BHs is well constrained by models, while the uncertainties about the normalisation are larger than the ones about Pop. III BBHs (e.g., Raidal et al. 2019; Vaskonen & Veermäe 2020; De Luca 2022), preventing us from drawing further conclusions. As discussed in Ng et al. (2022b), the Einstein Telescope and Cosmic Explorer might be able to disentangle the two populations of mergers by looking

at the overall shape of the merger rate density evolution. Additional information will come from the mass distribution of BBH mergers at high redshift (e.g., Franciolini et al. 2022).

5 SUMMARY AND CONCLUSIONS

We estimated the merger rate density evolution of binary black holes (BBHs) born from Pop. III stars (Figure 3) by means of our code `COSMORATE` (Santoliquido et al. 2021). To evaluate the main uncertainties affecting the merger rate density, we explored a large portion of the parameter space, making use of four different models for the formation history of Pop. III stars (from Jaacks et al. 2019, J19, Liu & Bromm 2020b, LB20, Skinner & Wise 2020, SW20, and Hartwig et al. 2022, H22), and eleven different configurations of the initial orbital properties of Pop. III binary stars. In particular, we probe different IMFs (flat-in-log, K01, L98, and top-heavy), mass ratios (S12, sorted), orbital period distributions (S12, SB13), and eccentricity distributions (S12, thermal), as described in Table 1. We generated the catalogues of Pop. III BBHs with our binary population-synthesis simulation code `SEVN` (Iorio et al. 2023), based on a new set of Pop. III stellar tracks with metallicity $Z = 10^{-11}$ and ZAMS mass $m_{\text{ZAMS}} \in [2, 600] M_{\odot}$ (Costa et al. 2023).

The assumed star formation rate history of Pop. III stars affects both the normalisation and the shape of the BBH merger rate density evolution with redshift (Fig. 3): $\mathcal{R}(z)$ peaks at $z_{\text{p}} \approx 8 - 10$ for the models by J19 and LB20, and at $z_{\text{p}} \approx 12 - 16$ for H22 and SW20. For our fiducial model LOG1, the maximum merger rate density ranges from $\mathcal{R}(z_{\text{p}}) \approx 30 \text{ Gpc}^{-3} \text{ yr}^{-1}$ for the star formation rate density (SFRD) by J19 down to $\mathcal{R}(z_{\text{p}}) \approx 2 - 4 \text{ Gpc}^{-3} \text{ yr}^{-1}$ for the SFRDs by SW20, H22, and LB20.

At redshift $z = 0$, all the considered SFRD models yield $\mathcal{R}(0) \leq 2 \times 10^{-1} \text{ Gpc}^{-3} \text{ yr}^{-1}$ in our fiducial model LOG1, about two orders of magnitude lower than the local BBH merger rate density inferred from LVK data (Abbott et al. 2023). Overall, changing the SFRD model for Pop. III stars affects the BBH merger rate density by up to about one order of magnitude. In the case of the SFRD derived by H22, we can also account for the intrinsic uncertainties of the SFRD calibration on data. We find that the merger rate density changes by about one order of magnitude within the 95% credible interval of the Pop. III SFRD estimated by H22 (Fig. 2).

The initial orbital properties of our Pop. III binary systems have an even larger impact on the BBH merger rate density, up to two orders of magnitude (Fig. 3). The models adopting a SB13 distribution for the initial orbital periods (LOG2, LOG5, KRO5, LAR5, and TOP5) have

lower merger rate densities than models adopting the distribution by S12 (LOG1, LOG3, LOG4, KRO1, LAR1, and TOP1). The reason is that short orbital periods, as in the case of S12, favour the merger of BBHs via stable mass transfer episodes between the progenitor stars, while large orbital periods (SB13) suppress these systems.

We estimated the mass distribution of Pop. III BBHs for all of our models as a function of redshift. Both the primary and secondary BH (i.e., the most and least massive member of a BBH) born from a Pop. III binary star tend to be substantially more massive than the primary and secondary BH born from a metal-rich binary star (Figs. 8, 9). This happens mainly because stellar winds are suppressed at low Z . The median mass of the primary BHs born from Pop. III stars is $m_1 \approx 30 - 40 M_\odot$ across the entire redshift range, while the median mass of primary BHs born from metal-rich stars is $m_1 \approx 8 M_\odot$ (Fig. 5). This result does not depend on the adopted SFRD and is only mildly sensitive to the initial orbital properties of Pop. III binary stars.

The mass spectrum of primary BHs inferred by the LVK (Abbott et al. 2023) is characterised by two peaks, the main one at $8 - 10 M_\odot$ and the other at $\sim 35 M_\odot$. The location of these two peaks is remarkably similar to the median mass of the primary BHs born from metal-rich and metal-free/metal-poor stars in our simulations.

The mass ratio q between the secondary and primary BH is another feature that distinguishes BBHs born from Pop. III and metal-rich binary stars (Fig. 7). Pop. III BBHs merging at low redshift ($z \leq 4$) have low mass ratios (median values $q \approx 0.5 - 0.7$) with respect to BBH mergers from metal-rich stars (median values $q \approx 0.9$). In contrast, at high redshift even BBH mergers born from Pop. III stars have a typical $q \sim 0.9$. This happens because the median secondary BH mass of Pop. III BBH mergers decreases with redshift. This feature is a consequence of the delay time distribution: Pop. III BBHs with relatively small secondary BH mass are associated with longer delay times than Pop. III BBHs with equal mass BHs (Fig. 11). This dependence of the delay time on the secondary BH mass is a consequence of the formation channels of our Pop. III BBHs. It is not affected by the adopted SFRD and is only mildly sensitive to the initial orbital properties of Pop. III binary stars, but it is highly sensitive to the assumed natal kick distribution. In our fiducial models, we assume that natal kicks are lower for more massive BHs and for (ultra-)stripped binary systems. If we instead use a natal kick model in which the kick magnitude does not depend on the properties of the system, the decrease of the median secondary BH mass with redshift almost disappears.

In our fiducial model (LOG1) and all the other models assuming the initial orbital period distribution by S12, most ($> 50\%$) of our Pop. III BBHs evolve via stable mass transfer episodes, without common envelope phases. This happens because the mass of Pop. III BHs is always sufficiently large with respect to the mass of the companion star to avoid common envelope (Costa et al. 2023).

Even if most of our BBH mergers from Pop. III stars are rather massive ($m_1 \approx 30 - 40 M_\odot$), BBHs with mass above or inside the pair-instability mass gap are extremely rare in our models. For example, assuming the SFRD by H22, we find that the local merger rate of Pop. III BBHs with primary BH mass $m_1 > 60 M_\odot$ is $< 10^{-4} \text{ Gpc}^{-3} \text{ yr}^{-1}$ in all of our models but LOG3, for which we find $\approx 4 \times 10^{-3} \text{ Gpc}^{-3} \text{ yr}^{-1}$.

Altogether, we expect that the Einstein Telescope will detect between 10 and 10^4 BBH mergers from Pop. III stars per year, depending on the adopted parameters. In particular, for our fiducial model (LOG1 with SFRD from H22) we expect ≈ 530 detections per year, of which 68% from BBH mergers occurring at redshift $z > 8$. Since the properties of low-redshift Pop. III BBH mergers are not dra-

matically different from those of BBHs originating from metal-rich stars, such high-redshift detections will be crucial to characterize the population of Pop. III BBHs. In a follow-up study, we will run parameter estimation on our simulated systems, to verify how well we can reconstruct their properties (mass and merger redshift) with the Einstein Telescope.

Our results show that the overall uncertainty on the merger rate density evolution of Pop. III BBHs mergers spans at least two orders of magnitude and depends on the SFRD model, initial orbital properties of Pop. III binary stars, and stellar/binary evolution physics. Future work should further explore the impact of stellar evolution (e.g., rotation, chemically homogeneous evolution, core overshooting) and different assumptions for mass and angular momentum evolution during mass transfer.

ACKNOWLEDGEMENTS

We thank the anonymous referee for their insightful comments which helped us improve this work. We are grateful to Stanislav Babak, Irina Dvorkin, Gabriele Franciolini, Cecilio García-Quirós, Tomoya Kinugawa, Natalia Korsakova, Paolo Pani, Federico Pozzoli, and Ataru Tanikawa for their enlightening comments. GC, GI, MM, and FS acknowledge financial support from the European Research Council (ERC) for the ERC Consolidator grant DEMOBLACK, under contract no. 770017. TH acknowledges financial support from JSPS (KAKENHI Grant Numbers 19K23437 and 20K14464) and the German Environment Agency. FS thanks the Astroparticule et Cosmologie Laboratoire (APC) and the Institute d’Astrophysique de Paris (IAP) for hospitality during the preparation of this manuscript. RSK and SCOG acknowledge financial support from the ERC via the ERC Synergy Grant “ECOGAL” (project ID 855130), from the German Excellence Strategy via the Heidelberg Cluster of Excellence (EXC 2181 - 390900948) “STRUCTURES”, and from the German Ministry for Economic Affairs and Climate Action in project “MAINN” (funding ID 50002206). RSK and SCOG also thank for computing resources provided by the Ministry of Science, Research and the Arts (MWK) of the State of Baden-Württemberg through bwHPC and the German Science Foundation (DFG) through grant INST 35/1134-1 FUGG and for data storage at SDS@hd through grant INST 35/1314-1 FUGG.

DATA AVAILABILITY

The main data presented in this work are publicly available on Zenodo at Santoliquido (2023). The latest public version of `sevn` can be downloaded from [this repository](#)³. `cosmoRATE` is publicly available on GitLab at [this link](#)⁴. Further data and codes will be shared on reasonable request to the corresponding authors.

REFERENCES

- Abbott B. P., et al., 2016a, *Phys. Rev. Lett.*, 116, 061102
 Abbott B. P., et al., 2016b, *ApJ*, 818, L22
 Abbott B. P., et al., 2019, *ApJ*, 882, L24
 Abbott R., et al., 2020a, *Phys. Rev. Lett.*, 125, 101102
 Abbott R., et al., 2020b, *ApJ*, 900, L13
 Abbott R., et al., 2021, *ApJ*, 913, L7

³ <https://gitlab.com/sevncodes/sevn.git>

⁴ https://gitlab.com/Filippo.santoliquido/cosmo_rate_public

- Abbott R., et al., 2023, *Physical Review X*, **13**, 011048
- Abel T., Bryan G. L., Norman M. L., 2002, *Science*, **295**, 93
- Ade P. A. R., et al., 2016, *A&A*, **594**, A13
- Aghanim N., et al., 2020, *A&A*, **641**, A6
- Alvarez M. A., Bromm V., Shapiro P. R., 2006, *ApJ*, **639**, 621
- Atri P., et al., 2019, *MNRAS*, **489**, 3116
- Ballone A., Costa G., Mapelli M., MacLeod M., Torniamenti S., Pacheco-Arias J. M., 2023, *MNRAS*, **519**, 5191
- Banerjee S., 2022, *A&A*, **665**, A20
- Belczynski K., et al., 2016, *A&A*, **594**, A97
- Belczynski K., Ryu T., Perna R., Berti E., Tanaka T. L., Bulik T., 2017, *MNRAS*, **471**, 4702
- Belczynski K., et al., 2020, *A&A*, **636**, A104
- Biver C. M., Capano C. D., De S., Cabero M., Brown D. A., Nitz A. H., Raymond V., 2019, *PASP*, **131**, 024503
- Blaauw A., 1961, *Bull. Astron. Inst. Netherlands*, **15**, 265
- Bouffanais Y., Mapelli M., Gerosa D., Di Carlo U. N., Giacobbo N., Berti E., Baibhav V., 2019, *ApJ*, **886**, 25
- Bouffanais Y., Mapelli M., Santoliquido F., Giacobbo N., Di Carlo U. N., Rastello S., Artale M. C., Iorio G., 2021, *MNRAS*, **507**, 5224
- Bray J. C., Eldridge J. J., 2016, *MNRAS*, **461**, 3747
- Bray J. C., Eldridge J. J., 2018, *MNRAS*, **480**, 5657
- Bressan A., Marigo P., Girardi L., Salasnich B., Dal Cero C., Rubele S., Nanni A., 2012, *MNRAS*, **427**, 127
- Broekgaarden F. S., et al., 2021, *MNRAS*, **508**, 5028
- Broekgaarden F. S., et al., 2022, *MNRAS*, **516**, 5737
- Bromm V., 2013, *Reports on Progress in Physics*, **76**, 112901
- Bromm V., Larson R. B., 2004, *ARA&A*, **42**, 79
- Bromm V., Loeb A., 2003, *Nature*, **425**, 812
- Bromm V., Yoshida N., Hernquist L., McKee C. F., 2009, *Nature*, **459**, 49
- Bryan G. L., et al., 2014, *ApJS*, **211**, 19
- Callister T. A., Farr W. M., 2023, *arXiv e-prints*, p. [arXiv:2302.07289](https://arxiv.org/abs/2302.07289)
- Chen H.-Y., Holz D. E., Miller J., Evans M., Vitale S., Creighton J., 2021, *Classical and Quantum Gravity*, **38**, 055010
- Chon S., Omukai K., Schneider R., 2021, *MNRAS*, **508**, 4175
- Choplin A., Tominaga N., Ishigaki M. N., 2019, *A&A*, **632**, A62
- Claeys J. S. W., Pols O. R., Izzard R. G., Vink J., Verbunt F. W. M., 2014, *A&A*, **563**, A83
- Costa G., Bressan A., Mapelli M., Marigo P., Iorio G., Spera M., 2021, *MNRAS*, **501**, 4514
- Costa G., Ballone A., Mapelli M., Bressan A., 2022, *MNRAS*, **516**, 1072
- Costa G., Mapelli M., Iorio G., Santoliquido F., Escobar G. J., Klessen R. S., Bressan A., 2023, *arXiv e-prints*, p. [arXiv:2303.15511](https://arxiv.org/abs/2303.15511)
- Crosby B. D., O'Shea B. W., Smith B. D., Turk M. J., Hahn O., 2013, *ApJ*, **773**, 108
- De Luca V., 2022, *arXiv e-prints*, p. [arXiv:2207.08638](https://arxiv.org/abs/2207.08638)
- De Luca V., Franciolini G., Pani P., Riotto A., 2020, *J. Cosmology Astropart. Phys.*, **2020**, 044
- Di Carlo U. N., Giacobbo N., Mapelli M., Pasquato M., Spera M., Wang L., Haardt F., 2019, *MNRAS*, **487**, 2947
- Di Carlo U. N., et al., 2020, *MNRAS*, **498**, 495
- Dominik M., et al., 2015, *ApJ*, **806**, 263
- Farag E., Renzo M., Farmer R., Chidester M. T., Timmes F. X., 2022, *ApJ*, **937**, 112
- Farah A. M., Edelman B., Zevin M., Fishbach M., María Ezquiaga J., Farr B., Holz D. E., 2023, *arXiv e-prints*, p. [arXiv:2301.00834](https://arxiv.org/abs/2301.00834)
- Farmer R., Renzo M., de Mink S. E., Fishbach M., Justham S., 2020, *ApJ*, **902**, L36
- Farrell E., Groh J. H., Hirschi R., Murphy L., Kaiser E., Ekström S., Georgy C., Meynet G., 2021, *MNRAS*, **502**, L40
- Finn L. S., Chernoff D. F., 1993, *Phys. Rev. D*, **47**, 2198
- Fishbach M., et al., 2021, *ApJ*, **912**, 98
- Franciolini G., Musco I., Pani P., Urbano A., 2022, *Phys. Rev. D*, **106**, 123526
- Fryer C. L., Belczynski K., Wiktorowicz G., Dominik M., Kalogera V., Holz D. E., 2012, *ApJ*, **749**, 91
- Gallegos-García M., Berry C. P. L., Marchant P., Kalogera V., 2021, *ApJ*, **922**, 110
- García-Quiros C., Colleonì M., Husa S., Estellés H., Pratten G., Ramos-Buades A., Mateu-Lucena M., Jaume R., 2020, *Phys. Rev. D*, **102**, 064002
- Giacobbo N., Mapelli M., 2019, *MNRAS*, **482**, 2234
- Giacobbo N., Mapelli M., 2020, *ApJ*, **891**, 141
- Giacobbo N., Mapelli M., Spera M., 2018, *MNRAS*, **474**, 2959
- Glover S., 2013, in Wiklind T., Mobasher B., Bromm V., eds, *Astrophysics and Space Science Library Vol. 396, The First Galaxies*. p. 103 ([arXiv:1209.2509](https://arxiv.org/abs/1209.2509)), doi:10.1007/978-3-642-32362-1_3
- Haiman Z., Thoul A. A., Loeb A., 1996, *ApJ*, **464**, 523
- Hartwig T., Volonteri M., Bromm V., Klessen R. S., Barausse E., Magg M., Stacy A., 2016, *MNRAS*, **460**, L74
- Hartwig T., et al., 2022, *ApJ*, **936**, 45
- Heger A., Woosley S., Baraffe I., Abel T., 2002, in Gilfanov M., Sunyaev R., Churazov E., eds, *Lighthouses of the Universe: The Most Luminous Celestial Objects and Their Use for Cosmology*. p. 369 ([arXiv:astro-ph/0112059](https://arxiv.org/abs/astro-ph/0112059)), doi:10.1007/10856495_57
- Hild S., Chelkowski S., Freise A., 2008, *arXiv e-prints*, p. [arXiv:0810.0604](https://arxiv.org/abs/0810.0604)
- Hild S., Chelkowski S., Freise A., Franc J., Morgado N., Flaminio R., DeSalvo R., 2010, *Classical and Quantum Gravity*, **27**, 015003
- Hild S., et al., 2011, *Classical and Quantum Gravity*, **28**, 094013
- Hirano S., Hosokawa T., Yoshida N., Umeda H., Omukai K., Chiaki G., Yorke H. W., 2014, *ApJ*, **781**, 60
- Hirano S., Hosokawa T., Yoshida N., Omukai K., Yorke H. W., 2015, *MNRAS*, **448**, 568
- Hobbs G., Lorimer D. R., Lyne A. G., Kramer M., 2005, *MNRAS*, **360**, 974
- Hopkins P. F., 2015, *MNRAS*, **450**, 53
- Hurley J. R., Tout C. A., Pols O. R., 2002, *MNRAS*, **329**, 897
- Inayoshi K., Hirai R., Kinugawa T., Hotokezaka K., 2017, *MNRAS*, **468**, 5020
- Iorio G., et al., 2023, *MNRAS*,
- Ishiyama T., Sudo K., Yokoi S., Hasegawa K., Tominaga N., Susa H., 2016, *ApJ*, **826**, 9
- Jaacks J., Finkelstein S. L., Bromm V., 2019, *MNRAS*, **488**, 2202
- Jaura O., Glover S. C. O., Wollenberg K. M. J., Klessen R. S., Geen S., Haemmerlé L., 2022, *MNRAS*, **512**, 116
- Johnson J. L., Greif T. H., Bromm V., 2007, *ApJ*, **665**, 85
- Kalogera V., et al., 2021, *arXiv e-prints*, p. [arXiv:2111.06990](https://arxiv.org/abs/2111.06990)
- Karlsson T., Johnson J. L., Bromm V., 2008, *ApJ*, **679**, 6
- Karlsson T., Bromm V., Bland-Hawthorn J., 2013, *Reviews of Modern Physics*, **85**, 809
- Kinugawa T., Inayoshi K., Hotokezaka K., Nakauchi D., Nakamura T., 2014, *MNRAS*, **442**, 2963
- Kinugawa T., Miyamoto A., Kanda N., Nakamura T., 2016, *MNRAS*, **456**, 1093
- Kinugawa T., Nakamura T., Nakano H., 2020, *MNRAS*, **498**, 3946
- Kinugawa T., Nakamura T., Nakano H., 2021, *MNRAS*, **501**, L49
- Kitayama T., Yoshida N., Susa H., Umemura M., 2004, *ApJ*, **613**, 631
- Klessen R. S., Glover S. C. O., 2023, *arXiv e-prints*, p. [arXiv:2303.12500](https://arxiv.org/abs/2303.12500)
- Kremer K., et al., 2020, *ApJ*, **903**, 45
- Kroupa P., 2001, *MNRAS*, **322**, 231
- Kruckow M. U., Tauris T. M., Langer N., Kramer M., Izzard R. G., 2018, *MNRAS*, **481**, 1908
- Larson R. B., 1998, *MNRAS*, **301**, 569
- Liu B., Bromm V., 2020a, *MNRAS*, **495**, 2475
- Liu B., Bromm V., 2020b, *MNRAS*, **497**, 2839
- Liu B., Bromm V., 2020c, *ApJ*, **903**, L40
- Madau P., Dickinson M., 2014, *ARA&A*, **52**, 415
- Madau P., Fragos T., 2017, *ApJ*, **840**, 39
- Madau P., Rees M. J., 2001, *ApJ*, **551**, L27
- Maeder A., Zahn J.-P., 1998, *A&A*, **334**, 1000
- Maggiore M., et al., 2020, *J. Cosmology Astropart. Phys.*, **2020**, 050
- Mandel I., Müller B., 2020, *MNRAS*, **499**, 3214
- Mandel I., de Mink S. E., 2016, *MNRAS*, **458**, 2634
- Mapelli M., 2016, *MNRAS*, **459**, 3432
- Mapelli M., Zampieri L., Ripamonti E., Bressan A., 2013, *MNRAS*, **429**, 2298
- Mapelli M., Spera M., Montanari E., Limongi M., Chieffi A., Giacobbo N., Bressan A., Bouffanais Y., 2020, *ApJ*, **888**, 76

- Marchant P., Langer N., Podsiadlowski P., Tauris T. M., Moriya T. J., 2016, *A&A*, **588**, A50
- Marchant P., Pappas K. M. W., Gallegos-Garcia M., Berry C. P. L., Taam R. E., Kalogera V., Podsiadlowski P., 2021, *A&A*, **650**, A107
- Marigo P., Girardi L., Chiosi C., Wood P. R., 2001, *A&A*, **371**, 152
- Mukherjee S., Dizgah A. M., 2022, *ApJ*, **937**, L27
- Mukherjee S., Silk J., 2021, *MNRAS*, **506**, 3977
- Mukherjee S., Meinema M. S. P., Silk J., 2022, *MNRAS*, **510**, 6218
- Neijssel C. J., et al., 2019, *MNRAS*, **490**, 3740
- Ng K. K. Y., Vitale S., Farr W. M., Rodriguez C. L., 2021, *ApJ*, **913**, L5
- Ng K. K. Y., et al., 2022a, *ApJ*, **931**, L12
- Ng K. K. Y., Franciolini G., Berti E., Pani P., Riotto A., Vitale S., 2022b, *ApJ*, **933**, L41
- Nguyen C. T., et al., 2022, *A&A*, **665**, A126
- Pavlovskii K., Ivanova N., Belczynski K., Van K. X., 2017, *MNRAS*, **465**, 2092
- Peters P. C., 1964, *Physical Review*, **136**, 1224
- Prole L. R., Clark P. C., Klessen R. S., Glover S. C. O., 2022, *MNRAS*, **510**, 4019
- Punturo M., et al., 2010, *Classical and Quantum Gravity*, **27**, 194002
- Raidal M., Spethmann C., Vaskonen V., Veermäe H., 2019, *J. Cosmology Astropart. Phys.*, **2019**, 018
- Regimbau T., et al., 2012, *Phys. Rev. D*, **86**, 122001
- Reitze D., et al., 2019, in *Bulletin of the American Astronomical Society*, p. 35 ([arXiv:1907.04833](https://arxiv.org/abs/1907.04833))
- Renzo M., Cantiello M., Metzger B. D., Jiang Y. F., 2020, *ApJ*, **904**, L13
- Riley J., Mandel I., Marchant P., Butler E., Nathaniel K., Neijssel C., Shortt S., Vigna-Gómez A., 2021, *MNRAS*, **505**, 663
- Sana H., et al., 2012, *Science*, **337**, 444
- Santoliquido F., 2023, *MNRAS*
- Santoliquido F., Mapelli M., Bouffanais Y., Giacobbo N., Di Carlo U. N., Rastello S., Artale M. C., Ballone A., 2020, *ApJ*, **898**, 152
- Santoliquido F., Mapelli M., Giacobbo N., Bouffanais Y., Artale M. C., 2021, *MNRAS*, **502**, 4877
- Santoliquido F., Mapelli M., Artale M. C., Boco L., 2022, *MNRAS*, **516**, 3297
- Schneider R., Ferrara A., Natarajan P., Omukai K., 2002, *ApJ*, **571**, 30
- Schneider R., Omukai K., Inoue A. K., Ferrara A., 2006, *MNRAS*, **369**, 1437
- Singh N., Bulik T., 2021, *Phys. Rev. D*, **104**, 043014
- Singh N., Bulik T., Belczynski K., Askar A., 2022, *A&A*, **667**, A2
- Skinner D., Wise J. H., 2020, *MNRAS*, **492**, 4386
- Spera M., Mapelli M., 2017, *MNRAS*, **470**, 4739
- Spera M., Mapelli M., Giacobbo N., Trani A. A., Bressan A., Costa G., 2019, *MNRAS*, **485**, 889
- Spruit H. C., 2002, *A&A*, **381**, 923
- Stacy A., Bromm V., 2013, *MNRAS*, **433**, 1094
- Stacy A., Bromm V., Lee A. T., 2016, *MNRAS*, **462**, 1307
- Susa H., Hasegawa K., Tominaga N., 2014, *ApJ*, **792**, 32
- Talon S., Zahn J. P., 1997, *A&A*, **317**, 749
- Tanikawa A., Kinugawa T., Yoshida T., Hijikawa K., Umeda H., 2021a, *MNRAS*, **505**, 2170
- Tanikawa A., Susa H., Yoshida T., Trani A. A., Kinugawa T., 2021b, *ApJ*, **910**, 30
- Tanikawa A., Chiaki G., Kinugawa T., Suwa Y., Tominaga N., 2022a, *PASJ*, **74**, 521
- Tanikawa A., Yoshida T., Kinugawa T., Trani A. A., Hosokawa T., Susa H., Omukai K., 2022b, *ApJ*, **926**, 83
- Tauris T. M., van den Heuvel E. P. J., 2006, in , Vol. 39, Compact stellar X-ray sources. pp 623–665
- Tauris T. M., et al., 2017, *ApJ*, **846**, 170
- Taylor S. R., Gerosa D., 2018, *Phys. Rev. D*, **98**, 083017
- Tegmark M., Silk J., Rees M. J., Blanchard A., Abel T., Palla F., 1997, *ApJ*, **474**, 1
- Tornatore L., Ferrara A., Schneider R., 2007, *MNRAS*, **382**, 945
- Uysal B., Hartwig T., 2023, *MNRAS*, **520**, 3229
- Valiante R., Schneider R., Volonteri M., Omukai K., 2016, *MNRAS*, **457**, 3356
- Vaskonen V., Veermäe H., 2020, *Phys. Rev. D*, **101**, 043015
- Vink J. S., Higgins E. R., Sander A. A. C., Sabhahit G. N., 2021, *MNRAS*, **504**, 146
- Volpato G., Marigo P., Costa G., Bressan A., Trabucchi M., Girardi L., 2023, *ApJ*, **944**, 40
- Wang L., Tanikawa A., Fujii M., 2022, *MNRAS*, **515**, 5106
- Wollenberg K. M. J., Glover S. C. O., Clark P. C., Klessen R. S., 2020, *MNRAS*, **494**, 1871
- Woosley S. E., 2017, *ApJ*, **836**, 244
- Woosley S. E., Heger A., 2021, *ApJ*, **912**, L31
- Woosley S. E., Heger A., Weaver T. A., 2002, *Reviews of Modern Physics*, **74**, 1015
- Yi S.-X., Nelemans G., Brinkerink C., Kostrzewa-Rutkowska Z., Timmer S. T., Stoppa F., Rossi E. M., Zwart S. F. P., 2022, *A&A*, **663**, A155
- Yoon S. C., Dierks A., Langer N., 2012, *A&A*, **542**, A113
- Yoshida N., Abel T., Hernquist L., Sugiyama N., 2003, *ApJ*, **592**, 645
- Yoshida N., Omukai K., Hernquist L., Abel T., 2006, *ApJ*, **652**, 6
- Ziosi B. M., Mapelli M., Branchesi M., Tormen G., 2014, *MNRAS*, **441**, 3703
- de Mink S. E., Mandel I., 2016, *MNRAS*, **460**, 3545
- du Buisson L., et al., 2020, *MNRAS*, **499**, 5941
- van den Heuvel E. P. J., Portegies Zwart S. F., de Mink S. E., 2017, *MNRAS*, **471**, 4256

APPENDIX A: COMPARISON SAMPLE OF BBHS FROM POP. I-II STARS

In Figures 5–9, we compare the masses of Pop. III BBHs with those of Pop. I-II BBHs. The latter are the fiducial model presented in Iorio et al. (2023). Here, we briefly summarise their main features but we refer to Iorio et al. (2023) for more details. We simulate 5M binary star systems⁵ for each of the following 15 metallicities: $Z = 10^{-4}$, 2×10^{-4} , 4×10^{-4} , 6×10^{-4} , 8×10^{-4} , 10^{-3} , 2×10^{-3} , 4×10^{-3} , 6×10^{-3} , 8×10^{-3} , 10^{-2} , 1.4×10^{-2} , 1.7×10^{-2} , 2×10^{-2} , 3×10^{-2} . The total number of simulated binary systems is thus 75M, ensuring that stochastic fluctuations are not important (Iorio et al. 2023).

The set-up of these simulations is the same as model KRO1, apart from the IMF mass range. In fact, we randomly draw the initial ZAMS mass of primary stars from a K01 IMF with $M_{\text{ZAMS},1} \in [5, 150] M_{\odot}$ instead of $[5, 550] M_{\odot}$. We randomly select the masses of secondary stars assuming the distribution of mass ratios from Sana et al. (2012) with a lower mass limit of $M_{\text{ZAMS},2} = 2.2 M_{\odot}$. The initial orbital periods and eccentricities are also generated according to the distributions by Sana et al. (2012). The set-up of `SEVN` is the same as we describe in Section 2.1.

From these simulations we extract our catalogues of Pop I and II BBH mergers, which we use as input conditions for `COSMORATE`. We calculate the merger rate density of these metal-rich BBHs in the same way as described in Section 2.4, and in particular in Equation 14. To calculate $\mathcal{S}(z', Z) = \psi(z') p(z', Z)$, in this case we use

$$\psi(z) = a \frac{(1+z)^b}{1 + [(1+z)/c]^d} [M_{\odot} \text{ yr}^{-1} \text{ Mpc}^{-3}], \quad (\text{A1})$$

where $a = 0.01 M_{\odot} \text{ Mpc}^{-3} \text{ yr}^{-1}$ (for a K01 IMF), $b = 2.6$, $c = 3.2$ and $d = 6.2$, from Madau & Fragos (2017).

We also assume an average metallicity evolution from Madau &

⁵ The fiducial model by Iorio et al. (2023) only contains 1M binary star systems for each metallicity. Here, we rerun the same model with a $5 \times$ higher statistics, to filter out stochastic fluctuations.

Fragos (2017):

$$p(z', Z) = \frac{1}{\sqrt{2\pi\sigma_Z^2}} \exp\left\{-\frac{[\log(Z(z')/Z_\odot) - \langle \log Z(z')/Z_\odot \rangle]^2}{2\sigma_Z^2}\right\}, \quad (\text{A2})$$

where $\langle \log Z(z')/Z_\odot \rangle = \log \langle Z(z')/Z_\odot \rangle - \ln(10)\sigma_Z^2/2$ and $\sigma_Z = 0.2$ (Bouffanaïs et al. 2021). Finally, in the calculation of the total initial stellar mass M_{TOT} , we introduce a term $M_{\text{TOT}} = M_{\text{sim}}/f_{\text{IMF}}$, where M_{sim} is the total initial simulated stellar mass and $f_{\text{IMF}} = 0.285$, to account for the fact that we simulate only stars with $M_{\text{ZAMS},1} > 5 M_\odot$ and $M_{\text{ZAMS},2} > 2.2 M_\odot$, but we expect the K01 IMF to extend down to $0.1 M_\odot$.

APPENDIX B: IMPACT OF MASS ACCRETION AND COMMON ENVELOPE EFFICIENCY

The models shown in the main text assume mass-accretion efficiency $f_{\text{MT}} = 0.5$ for a non-degenerate accretor, and common-envelope efficiency $\alpha = 1$. Here, we show the results of some additional models, in which we vary both f_{MT} and α . In particular, we fix the initial binary orbital parameters to model LOG1 (Table 1) and the star-formation history to H22, and we explore the cases with $f_{\text{MT}} = 0.1, 0.5, 1.0$ for a non-degenerate accretor, and $\alpha = 0.5, 1, 3$. The model with $\alpha = 1$ and $f_{\text{MT}} = 1$ is the same as model LOG1 in Fig. 2.

A low value of f_{MT} (highly non-conservative mass transfer) leads to higher merger rates at lower redshift, and is almost insensitive to the choice of α (Fig. B1). This happens because the mass of the secondary star does not grow much during the first mass-transfer episode; when the primary star becomes a BH, the mass ratio between the companion star and the BH is never large enough to trigger a common envelope. Moreover, the binary system loses angular momentum because of mass loss and its semi-major axis shrinks: the progenitor binary star steadily evolves via stable mass transfer and the resulting BBH merges with a long delay time.

In contrast, relatively large values of f_{MT} lead to an efficient mass growth of the secondary star, increasing the chances that the system undergoes a common envelope episode (Fig. B1). Larger values of α favour the ejection of the envelope and permit the survival of the binary system, whereas lower values of α trigger collisions between the star and the BH (or between the two progenitor stars), reducing the BBH merger rate density.

Such differences have a mild impact on the distribution of the primary mass (Fig. B2). BBHs with primary mass above the gap have a higher merger efficiency in the simulations with $\alpha = 0.5$ at low redshift. These systems evolve via channel III: their orbital separation shrinks more efficiently with $\alpha = 0.5$, allowing them to merge even if they have large initial orbital periods.

Figure B1 also shows the comparison between our fiducial model (LOG1) and a simulation (QCBSE) in which we use the same mass-transfer stability criteria as Hurley et al. (2002). The main difference between LOG1 and QCBSE is that the former assumes that mass transfer is always stable for donor stars in the main sequence and Hertzsprung-gap phase, while the latter allows for mass transfer to become unstable in these early evolutionary phases. We find almost no difference between LOG1 and QCBSE, because the progenitors of most of our successful BBH mergers undergo the first mass transfer episode when the primary star is a post-Hertzsprung gap object.

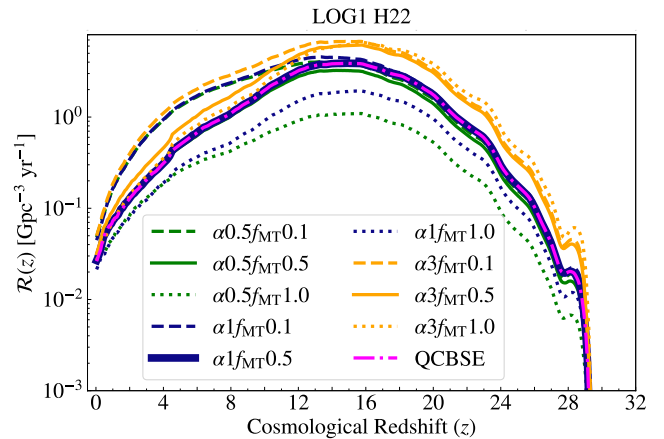


Figure B1. BBH Merger rate density evolution assuming the star formation rate history from H22 and the initial binary orbital parameters as in model LOG1 (Table 1). Dashed, solid and dotted lines refer to models with mass-accretion efficiency $f_{\text{MT}} = 0.1, 0.5$, and 1 , respectively. Green, blue and yellow lines refer to models with $\alpha = 0.5, 1$ and 3 , respectively. The thick solid blue line (with $f_{\text{MT}} = 0.5$ and $\alpha = 1$) is the same as model LOG1 (solid blue line) in Fig. 2. Finally, the dot-dashed magenta line (model QCBSE) is the same as the solid blue line but adopts the mass-transfer stability criteria by Hurley et al. (2002).

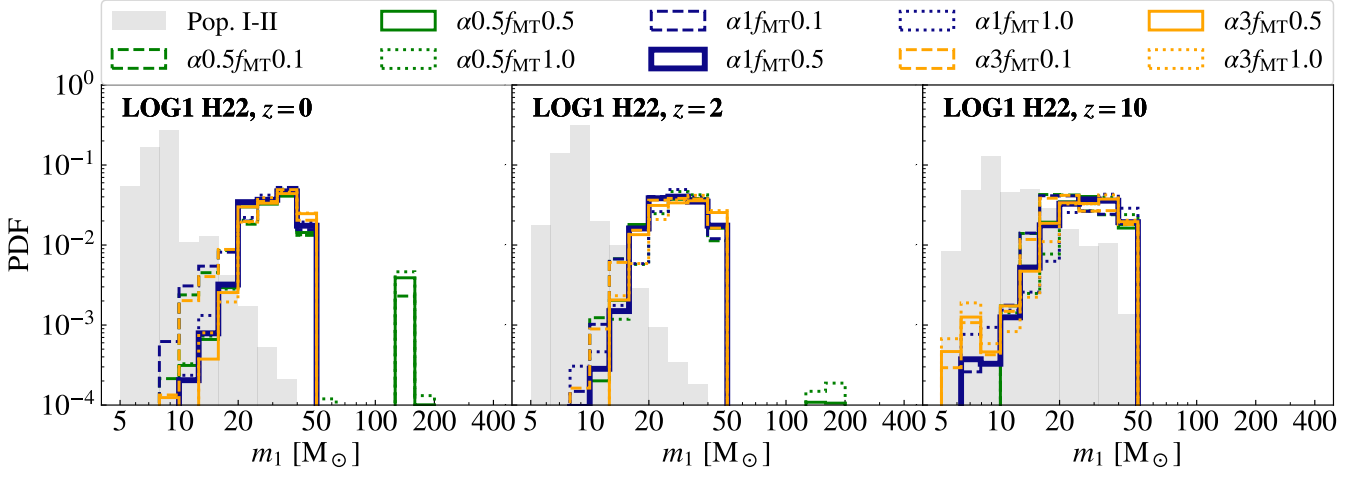


Figure B2. Primary BH mass distribution of Pop. III BBHs merging at redshift $z = 0$, (left), 2 (middle), and 10 (right) assuming the star formation history from **H22** and the initial binary orbital parameters as in model LOG1 (Table 1). Dashed, solid and dotted lines refer to models with mass-accretion efficiency $f_{\text{MT}} = 0.1, 0.5$, and 1, respectively. Green, blue and yellow lines refer to models with $\alpha = 0.5, 1$ and 3, respectively. The grey shaded histogram shows the distribution of Pop. I-II BHs for comparison. The model QCBSE (magenta line in Fig. B1) is not shown here, because it perfectly overlaps with model LOG1 (thick solid blue line).